

Probing of magnetic dimensional crossover in CrSiTe_3 through picosecond strain pulses

Anjan Kumar N M¹, Soumya Mukherjee¹, Abhirup Mukherjee¹, Ajinkya Punjal², Shubham Purwar³, Thirupathaiah Setti³, Shriganesh Prabhu S², Siddhartha Lal¹, N. Kamaraju^{1*}

Corresponding authors email : nkamaraju@iiserkol.ac.in

¹ Department of Physical Sciences, Indian Institute of Science Education and research, Kolkata, 741246, West Bengal, India.

² Department of Condensed Matter Physics and Materials Science, Tata Institute of Fundamental research, Mumbai, 400005, Maharashtra, India.

³ Department of Condensed Matter and Materials Physics, S. N. Bose National Centre for Basic Sciences, Kolkata, 700 106, West Bengal, India

Abstract

Elucidating the emergence of long-range magnetic ordering from its precursor short-range magnetic ordering (SRMO) in two-dimensional van der Waals materials holds profound implications for fundamental research and technological advancements. However, directly observing the intricate stages of this magnetic dimensional crossover (MDC) remains a significant experimental challenge. While magneto-elastic coupling offers a promising avenue, detecting the minute lattice response to SRMO proves challenging. Recent investigations utilizing second harmonic generation have unveiled a two-step MDC in a van der Waals ferromagnetic insulator. However, an unambiguous detection of MDC through the time-resolved techniques remains elusive. To meet this goal, we have executed an alternative approach by employing picosecond acoustic strain pulses generated by femtosecond lasers to probe the various stages of MDC through the magneto-elastic coupling for the first time. By analyzing the shape of the strain pulse in both the time and frequency domains as a function of temperature, we clearly demonstrate the detection of the subtle influence of spin fluctuations on the lattice. Additionally, the ultrafast carrier dynamics also show signatures of MDC. Our measurements pave the way towards characterizing magnetic materials in time-resolved experiments that are crucial in designing a new generation of spin-based optoelectronic devices.

Introduction

Unveiling the impact of long-range magnetic ordering (LRMO) on lattice, charge, and orbital degrees of freedom in magnetic materials is crucial from both basic and technological standpoints[1, 2]. There has been a surge of interest in understanding the multistep process by which spin fluctuations drive the magnetic dimensional crossover in van der Waals materials[3, 4, 5] from two-dimensional (2D) short-range magnetic ordering to three-dimensional LRMO. Such a MDC is necessitated by the Mermin–Wagner–Hohenberg theorem[6, 7]. Recently, a two-step MDC has been detected in a van der Waals ferromagnetic (FM) Insulator with strong magneto-elastic coupling, CrSiTe₃, using second harmonic generation (SHG) experiments[8] that are sensitive to minute atomic distortions. The MDC is observed to proceed from a high-temperature paramagnetic phase with 2D SRMO fluctuations to a low-temperature three-dimensional (3D) ferromagnetically ordered phase, through an intervening phase that displays 2D magnetic LRMO fluctuations. Since the atomic distortions caused by SRMO are difficult to detect in X-ray, neutron, and optical scattering, studies have typically been carried out using Raman active modes [1, 2]. A recent investigation using ultrafast time-resolved measurements[16] has examined the influence of SRMO fluctuations on coherent A_g³ optical phonon. However, achieving a clear detection of the entire voyage of magnetic dimensional crossover (MDC) through its various stages using time-resolved techniques continues to be a challenge.

Here, we study the influence of strong magnetoelastic coupling in CrSiTe₃ by employing ultrafast femtosecond pulses to generate a stress composed of thermoelastic [12], electronic [11] and magnetic origin [14, 15] in addition to producing photoexcited carriers[16, 17]. In turn, this stress generates a picosecond acoustic strain pulse that will be sensitive to MDC in magnetic materials. Tracking the picosecond acoustic strain pulse in both the frequency and time domains, as a function of temperature, we detect the various stages of MDC. Additionally, we observe that the ultrafast dynamics of the photoexcited carriers too show signatures of MDC. Consequently, the findings of this study offer a valuable tool for examining the influence of magnetic ordering on the dynamics of photoexcited carriers, a critical aspect in the development of novel spin-based optoelectronic devices. To the best of our knowledge, this is the first time such a method has been employed to investigate MDC in magnetic materials.

In this work, the ultrafast dynamics of photoexcited electrons and the generated strain pulse characteristics are investigated in bulk CrSiTe₃ at various temperatures using a non-degenerate pump-probe technique(see Fig. 1(a) for the schematic). The transient differential reflectivity data reveal a pump-induced acoustic strain pulse superimposed on an exponentially decaying electronic background. The relaxation timescales and coefficients extracted from multiexponential data fitting to the electronic background decay exhibit a significant change around the temperature T_{3D} ~ 50 K, where the onset of LRMO fluctuations begins [8]. In addition, the shape of the acoustic strain pulses exhibits a continuous change across each stage of magnetic dimensional crossover. By analyzing the strain pulses in the frequency domain, it becomes evident that the onset of LRMO fluctuations, brought about by the emergence of interlayer spin-spin interactions, impacts the acoustic strain pulses. This impact manifests itself as a softening of the high-frequency acoustic part by ~ 6 GHz and a gapping out of the low-frequency acoustic part by ~ 7 GHz. Both these behaviors

and the change in the phase of the strain pulse are effectively captured by our phenomenological model, which takes into account the coupling of magnetic interactions, with lattice distortion and its gradient.

Experiments & Results

CrSiTe₃ is a layered ferromagnet with Cr atoms forming honeycomb lattices. The ferromagnetic exchange interactions between the Cr ions result in spontaneous LRMO below the Curie temperature of 33 K (refer to Fig. 1 (b)), with the easy axis aligned along the c-axis [1, 18]. The commencement of the LRMO fluctuations through the interlayer spin-spin interaction is known to begin at ~ 60 K based on SHG investigations[8]. Inelastic neutron scattering experiments have revealed that CrSiTe₃ has intralayer spin-spin correlations even up to 300K, which are prominent below ~ 110 K[18]. As a result, the temperature at which the in-plane spin-spin interaction appears is denoted as T_{2D} . The multi-step energetics to establish the LRMO in CrSiTe₃ [8], and the presence of strong spin-lattice coupling[1, 2], makes this material an ideal test bed to investigate the spin-spin correlations and its effect on the lattice using picosecond acoustic strain pulses(see Fig. 1 (c)). The various processes listed in Fig. 1(c) will be discussed further in the experimental results.

In this ultrafast pump probe experiment, an ultrashort visible pulse (~ 60 fs, ~ 1.9 eV) excites the sample by transferring the electrons directly from Te 5p level to Cr 3d level (see Supplementary Sect. II and Fig. S6). This charge transfer significantly enhances the ferromagnetic super-exchange interaction between the Cr³⁺ metal ions, which are mediated by a nonmagnetic Te ligand[16]. To gauge pump-induced changes, a probe pulse with a photon energy centered at ~ 1.55 eV is used to measure the transient differential reflectivity (DR) at various temperatures ranging from 4 K to 300 K. The temperature evolution of the raw DR data is shown in Fig. 2(a) as a two dimensional (2D) false colour plot (refer to Supplementary Fig. S5(a-c) for the complete data). The raw DR data shows an abrupt change near the Curie temperature ($T_c \sim 33$ K, refer Fig. 2(a)). The photoinduced DR data is positive after the pump pulse excites the electrons to the excited state (refer to Supplementary Fig. S 5(b-c)). These photoexcited electrons exchange energy with the spin and lattice subsystems, each with a characteristic relaxation timescale reflected in the exponential decay of the DR data background. On top of the exponentially decaying background the raw DR data has a strain pulse (refer to Supplementary Fig. S 5(b-c)). The decaying exponential part of the DR data could be successfully fitted with the multi-exponential functions. It should be noted that a minimum sum of three exponentials is required to fit the data taken up to the temperature of 35K, whereas, only two exponentials are sufficient to fit the exponential background of DR data taken at the temperatures $T > 35$ K (refer to Supplementary Fig. S7(a-b)). The fact that the electronic background of DR is found to be fitted with a different number of exponentials across 35 K suggests that LRMO or the onset of LRMO fluctuations influence the electron dynamics in CrSiTe₃. To further assert our claim, we examine the effect of the spin fluctuations on the decay time constants and the decay coefficients of the electronic background. The decay time constants extracted from the multi-exponential fitting to the electronic background and its variations with the temperature is shown in Fig. 2(b). The associated decay coefficients are shown in Supplementary Fig. S9.

The values of the extracted decay time constants($\tau_1 \sim 1 - 3$ ps , $\tau_2 \sim 15$ ps, $\tau_3 \sim 100 - 200$

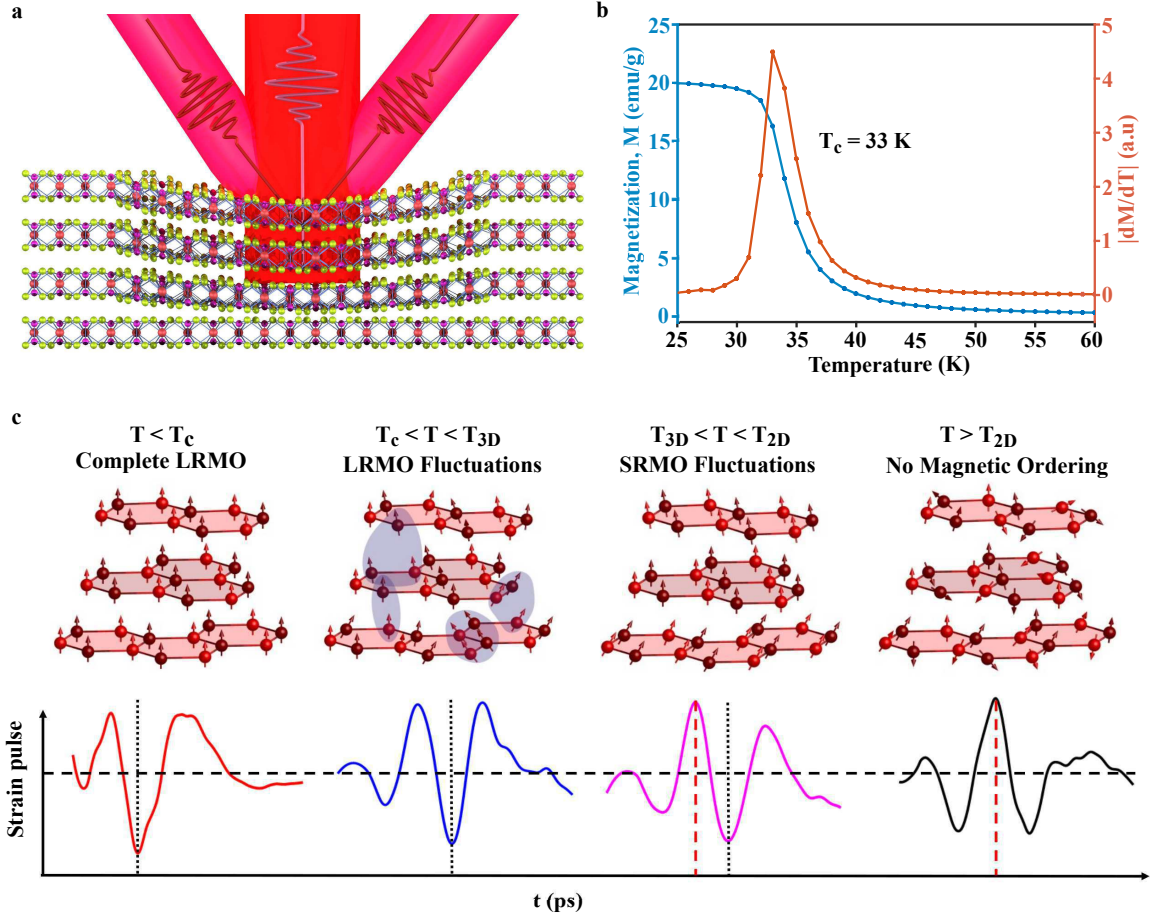


Figure 1: Detection of dimensional crossover using strain pulses: (a) Schematic of ultrafast pump probe technique to generate and detect the strain pulse (b) Variation of magnetization as a function of temperature (blue filled hexagons are the data and the blue lines are the guide to the eye) and absolute value of derivative of magnetization (dM/dT) versus temperature (orange lines are the guide to the eye, connecting the orange filled hexagons(data)). Transition temperature is found here to be 33 K, (c) The various stages of magnetic ordering captured by the strain pulse, depicted along with the schematic of 'Cr' spin ordering in the layers. One can notice that the maximum of the strain pulse is negative at $T < T_c$ and the shape of the strain pulses gradually changes to a stage where the maximum of the pulse becomes positive at $T > T_{2D}$. The horizontal black dashed line denotes the reference level ($y = 0$). Vertical lines, distinguished by dotted and dashed styles, identify the extrema of the strain pulses. The red dashed line marks the tensile strain (positive peak), while the black dotted line marks the compressive strain (negative peak). Note that at $T > T_{2D}$, the maxima and minima are comparable and hence both extremas are marked.

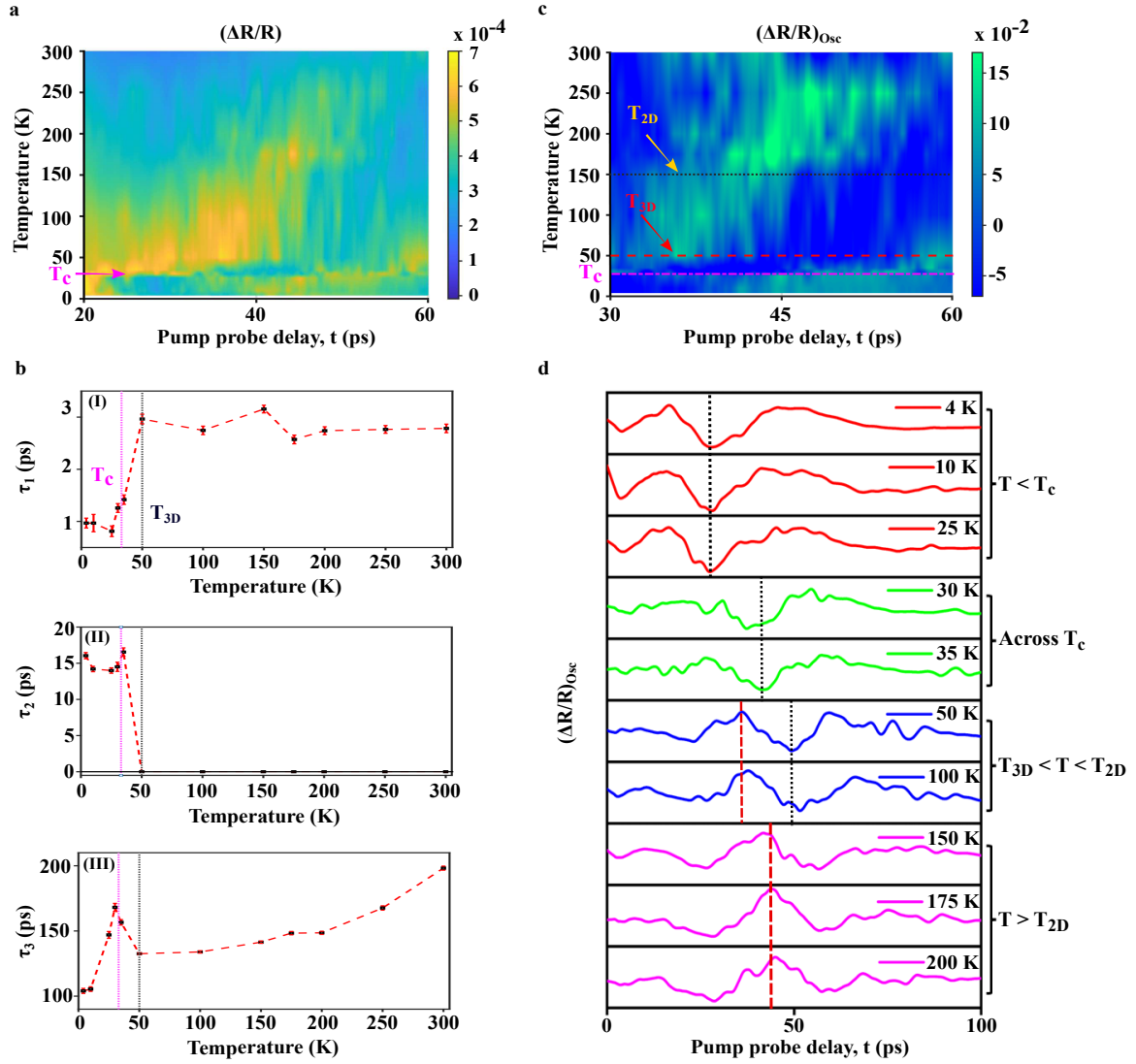


Figure 2: Effect of magnetic order on the carrier dynamics and the strain pulses: (a) A 2D false color plot of temperature dependent evolution of raw transient reflectivity data. Curie temperature (T_c) is indicated in solid red arrow. For clarity, the data is shown up to the pump probe delay time from 20 ps to 60 ps. (b) relaxation timescales extracted from a multi-exponential fit to the transient differential reflectivity data are shown as black squares, with error bars determined using orthogonal distance regression (ODR) approach. The red dotted lines are guides to the eye. The vertical magenta and black solid lines indicate the Curie temperature (T_c) and the temperature (T_{3D}) at which the onset of LRMO begins, respectively. (c) A 2D false color map of strain pulses is shown as a function of pump-probe delay and temperature. The horizontal black dotted line, red dashed line, and magenta dot-dashed line mark the temperatures T_{2D} , T_{3D} , and T_c , respectively. For clarity, the data is shown up to the pump probe delay time of 30 ps to 60 ps (d) The extracted strain pulses from DR data at various temperatures are shown in different colors. Red, green, blue and magenta solid lines represent strain pulses at temperatures $T < T_c$, across T_c , $T_{3D} < T < T_{2D}$ and $T > T_{2D}$, respectively. Vertical lines, distinguished by dotted and dashed styles, identify the extrema of the strain pulses. The red dashed lines mark the maximum tensile strain (positive peak), while the black dotted lines mark the minimum compressive strain (negative peak)

ps), are well-separated and can be attributed to different physical processes as discussed below. The pump pulse starts the Te - Cr charge transfer process by creating hot electrons in the conduction band. These hot electrons then thermalize through electron-electron interactions and then exchange energy with the lattice and spin degrees of freedom. The fastest relaxation timescale, τ_1 , which is shown in Fig. 2(b), increases from ~ 1.5 ps to ~ 3 ps as the temperature rises from 4 K to 50 K, and it is nearly independent of temperature above 50 K to 300 K. This decay is attributed to electron-phonon thermalization [19]. As τ_1 is ~ 1.5 ps below 50 K and 3 ps above 50 K, it indicates that an extra scattering channel is activated below $T_{3D} \sim 50$ K, and this could be the spin channel [19, 20, 21].

Subsequent to the energy exchange between the electron and phonon subsystems, the lattice-spin coupling induces an additional energy and angular momentum exchange between the lattice and spins [22, 16, 23]. This process is characterized by the relaxation timescales τ_2 and τ_3 . The timescale τ_2 , emerging only below 50 K (T_{3D}), suggests a link to the interaction of phonons with interlayer spin-spin fluctuations. The value of approximately 16 ps for τ_2 aligns with the typical time scales of spin-lattice interaction observed in another 2D ferromagnetic van der Waals material, Fe_3GeTe_2 [23, 24]. On the contrary, the time scale τ_3 ranges from 100 to 200 ps and shows a peak at the Curie temperature (T_c). This third timescale is attributed to the lattice interaction with the intralayer spin-spin fluctuations, in keeping with the observation of a divergence in the intralayer spin-spin correlation length at T_c in neutron diffraction studies [18]. Furthermore, τ_3 increases as the sample is heated up: this is likely due to the decrease in the strength of intralayer spin-spin correlations and a concomitant reduction in its interaction with the lattice. Thus, CrSiTe_3 exhibits two distinct lattice-spin coupling mechanisms: one linked to the interlayer spin-lattice interaction (which is dominant below 50 K) and another originating from the intralayer spin-lattice interaction. Both highlight the complex interplay between lattice and spin dynamics in this material. Alongside the triexponential function, there exists a constant background (A_0) and this can be attributed to a long electron-hole recombination time. A_0 also shows a peak at T_c (see Supplementary Fig. S9 (d)), suggesting that the electron-hole recombination process is affected by magnetic ordering [25].

Next, we turn our attention to the intriguing oscillatory part of the DR data. We retrieve the strain pulse (oscillatory component) by subtracting the multi-exponential electronic background at each temperature. The 2D contour plot of time dependent strain pulses is shown in Fig. 2 (c). The essential aspect to consider here is the effect of temperature on the shape of the strain pulse. Figure 2(d) depicts evolution of the time domain strain pulses (smoothened data for clarity, see Supplementary Sec. IV and Fig. S11) at different temperatures upto 200 K. The raw data at all temperatures is shown in Supplementary Fig. S10. From Fig. 2(d) it is evident that every stage of the spin-spin correlations (dimensional crossover) is affecting the shape of the strain pulse. In particular, the strain pulse in the ferromagnetic (FM) phase (red solid lines in Fig. 2 (d)) is inverted compared to the strain pulse in the paramagnetic (PM) phase (magenta solid lines in Fig. 2 (d)). For the clarity the data at FM (4K) and PM (150 K) phases is shown in the Supplementary Fig. S12.

The shape of strain pulses produced by femtosecond pulses in semiconductors is influenced by the interplay between thermoelastic (TE) and deformation potential (DP) induced stresses [12, 11, 14, 15]. These stresses produce a bipolar strain pulse with a leading compressive and a trailing tensile part. When a femtosecond pulse is shone on a magnetic semiconductor such as CrSiTe_3 ,

magnetic stresses are also produced in addition to TE and DP induced stresses. This magnetic stress generate a contractive strain pulse [14, 15]. The inversion of the strain pulse in the ferromagnetic phase compared to the paramagnetic phase suggests an interplay between these different generation processes: i.e, in FM phase, the strain pulse has a more negative amplitude than the positive amplitude, while in the PM phase, the positive amplitude dominates the negative amplitude (refer to Supplementary Fig. S12). We provide an explanation of the inversion of the strain pulse below based on a phenomenological model of spin-lattice coupling. To quantify the interplay between these processes, the difference in the peak-to-peak value (ΔP) of the strain pulses and the area under central part of the strain pulse (ΔA) are extracted (The extraction process is depicted in the Supplementary Fig. S13). Both ΔP and ΔA , show a similar trend with temperature in Fig. 3 (a). In Fig. 3 (a), $\Delta F(T)$ represents both ΔP and ΔA as a function of temperature (T). $\Delta F(T)$ decreases with decreasing temperature, especially below 150K, and changes sign around a temperature of $T_{3D} \sim 50$ K. This behavior can be explained as follows: In the paramagnetic phase, the positive $\Delta F(T)$ indicates a dominance of positive strain contributions, indicating the lattice expansion. This expansion results from elastic stresses induced by the TE and DP processes. Upon cooling, below 150 K, the strengthening spin-spin correlations generate a contractive strain pulse through the magnetostriction effect. This counteracts the elastic expansive stress, diminishing the positive portion of $\Delta F(T)$. Furthermore, below 50 K, the emergence of long-range magnetic order (LRMO) fluctuations leads to a non-zero net magnetization (M). This non-zero magnetization further enhances the contractive strain pulse, causing $\Delta F(T)$ to exhibit a negative sign. Supporting these observations, studies on magnetic thin films with optical pump-X-ray probe methods have hinted at the interplay between elastic and magnetic stresses[13, 14, 18].

To understand these observations further, we resort to Fourier and wavelet analysis of the time domain strain data. The continuous wavelet transform (CWT) effectively captures the evolution of the temperature-dependent frequency spectrum at various pump-probe time delays (Refer to Supplementary section V). Figure 3(b) presents the temperature evolution of the frequency spectrum (normalized with respect to the peak amplitude obtained from wavelet analysis) at the pump probe delay time, $t = 60$ ps, as a 2D false color plot (refer to the Supplementary Figs. S15 and S16 for the evolution of the CWT spectrum at various pump probe delay times and at various temperatures). For clarity, smoothened frequency spectra obtained from Fourier transform at four temperatures are shown in Fig. 3(c). The frequency spectrum has two parts: a high-frequency acoustic part (HFAP) and a low-frequency acoustic part (LFAP). The HFAP's central frequency undergoes a significant renormalization, dropping from 33 GHz to 27 GHz (marked by the double red arrow in Fig. 3(b)). Below T_{3D} , it softens markedly and exhibits a red shift above T_{3D} . On the contrary, the LFAP emerges above T_{3D} and shows a weak temperature dependence. Interestingly, below T_{3D} , the LFAP undergoes a blue shift by 7 GHz (toward higher frequencies), which leads to its disappearance (gapping out) within this temperature regime.

The influence of spin-spin correlations on the shape and the frequency of the strain pulse observed by us can be elucidated by employing a phenomenological model Lagrangian given by,

$$\mathcal{L} = \sum_j \left[\dot{Q}_j^2 - \lambda(Q_{j+1} - Q_j)^2 + \gamma \vec{S}_j \cdot \vec{S}_{j+1} Q_j - \xi \vec{S}_j \cdot \vec{S}_{j+1} Q_j^2 + \chi \vec{S}_j \cdot \vec{S}_{j+1} (Q_{j+1} - Q_j)^2 \right] \quad (1)$$

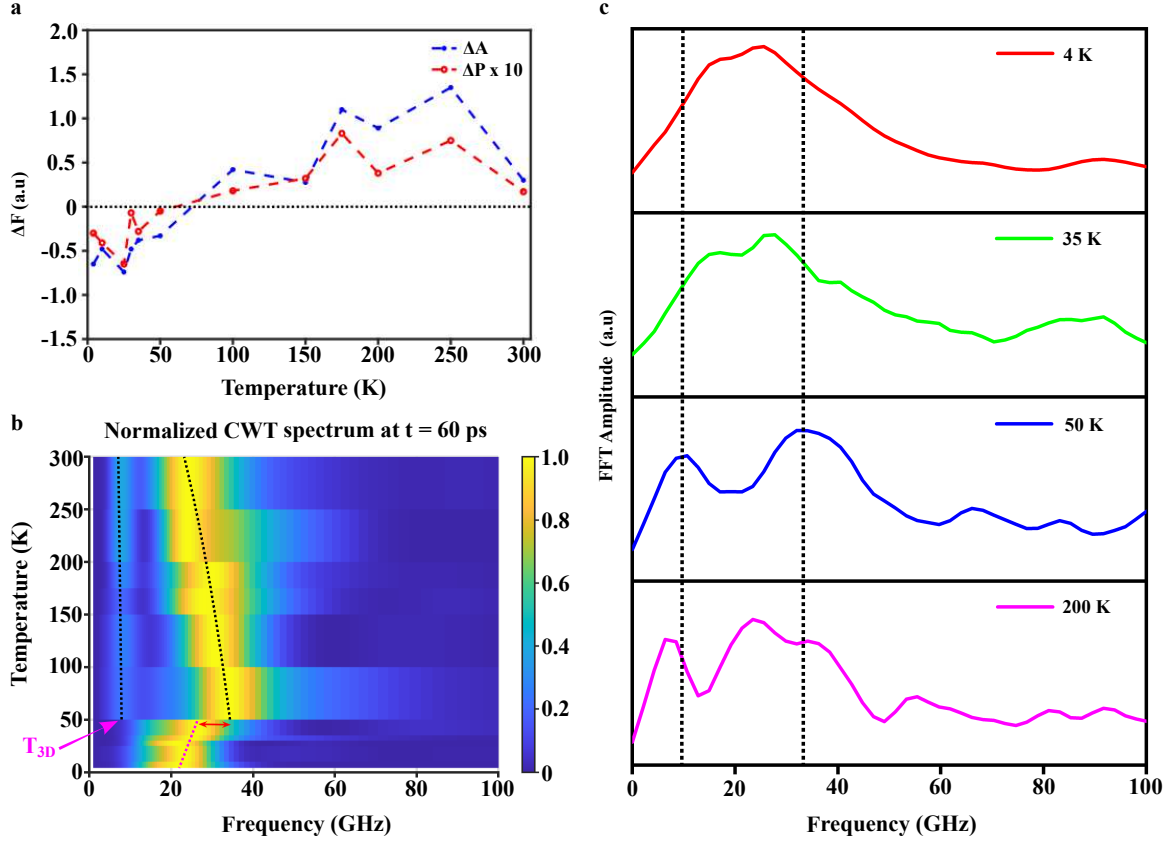


Figure 3: (a) The variation of the difference in the peak-to-peak value (ΔP) of the strain pulses and the difference in the area under the curve of the positive and negative sides of the strain pulse (ΔA) as a function of temperature. For the clarity, both (ΔP) and (ΔA) are represented as $\Delta F(T)$, and (ΔP) is scaled up by a factor of 10. (b) The 2D false color map of evolution of the frequency spectrum obtained by continuous wavelet transform of the strain pulse with the temperature at the pump probe delay time of 60 ps. The data is normalized with respect to its peak value and shown up to 100 GHz for clarity. The variation in frequency of LFAP and HFAP with the temperature above the onset of LRMO temperature $T_{3D} \sim 50$ K is fitted with the anharmonic decay model and is shown here as the dotted black lines. The dotted red lines are guide to the eye, to indicate the softening of HFAP below T_{3D} . A solid red double arrow depicts the shift in the central frequency of HFAP across T_{3D} . (c) This plot shows Fourier-transformed frequency spectra at four temperatures (only 4 data are shown here for clarity). Data are smoothed for better visualization without affecting peak frequencies. Vertical dotted lines mark the central frequencies of LFAP and HFAP, shown relative to the 50 K spectrum. Noticeably, above $T_{3D} = 50$ K, both peaks redshift (move towards lower frequencies). However, below T_{3D} , HFAP red-shifts while LFAP blue-shifts (moves towards higher frequencies). Our main text explains this contrasting behavior through spin-lattice coupling.

The first two terms of the Lagrangian represents the lattice model of phonons, where Q_j is the distortion of the j^{th} atom away from its equilibrium position, and λ is the spring constant of the restoring potential. The distortions $Q_j(t)$ are functions of the position index j as well as time t . The Lagrangian includes additional terms that describe the interaction between lattice distortions and magnetic interactions. These magnetic interactions are assumed to be of the nearest-neighbor kind $\vec{S}_j \cdot \vec{S}_{j+1}$, and they can couple to the linear, quadratic, and gradient components of the distortion, represented by Q_j , Q_j^2 and $(Q_{j+1} - Q_j)^2$, through the coupling constants γ , ξ and χ , respectively.

In this approach, the magnetic interactions are treated at the mean-field level and are replaced by their expectation values. This leads to the correlation $\langle \vec{S}_j \cdot \vec{S}_{j+1} \rangle$ acquiring a uniform non-zero value $M^2(T)$, where M is the magnetization. When the temperature exceeds T_{3D} , $M^2(T)$ becomes zero. The Lagrangian for the LRMO phase takes the form

$$\mathcal{L} = \sum_j \left[\dot{Q}_j^2 - (\lambda - M^2\chi)(Q_{j+1} - Q_j)^2 - M^2\xi \left(Q_j - \frac{\gamma}{2\xi} \right)^2 \right] \quad (2)$$

where we have neglected the overall constant.

We define a modified distortion $\bar{Q}_j = Q_j - \frac{\gamma}{2\xi}$. In terms of the modified distortion the Lagrangian becomes,

$$\mathcal{L} = \sum_j \left[\dot{\bar{Q}}_j^2 - (\lambda - M^2\chi)(\bar{Q}_{j+1} - \bar{Q}_j)^2 - M^2\xi \bar{Q}_j^2 \right] \quad (3)$$

The above Lagrangian yields the phonon dispersion relation given by,

$$\omega(k) = \sqrt{(\lambda - M^2\chi)k^2 + M^2\xi} \quad (4)$$

where k is the phonon wave-vector. As a consequence, when M is zero (for $T > T_{3D}$), the dispersion reduces to the linear form expected for acoustic phonons: $\omega(k) = \sqrt{\lambda}k$. When M and the coupling χ are nonzero (for $T < T_{3D}$) but the coupling ξ is negligible, the dispersion has the same form, but the spring constant λ is reduced, leading to softening of the mode.

$$\omega(k) = \sqrt{\lambda_{eff}}k, \quad \lambda_{eff} = \lambda - M^2\chi. \quad (5)$$

Therefore, the coupling between the spin-spin correlations and the gradient component of the distortions leads to the softening of the HFAP across T_{3D} for the case $M^2\chi < \lambda$.

When M , χ and ξ are all non-zero (for $T < T_{3D}$), the dispersion relation takes the form of equation (4) which indicates that the coupling between the spin-spin correlations and the quadratic component of the distortions can lead to the gapping out of the acoustic modes below T_{3D} making it harder to observe. This captures the onset of long-range magnetic order (LRMO) fluctuations below T_{3D} observed by us. The observed frequency shift between 50 K and 35 K, with a blue shift of about 7 GHz for LFAP and a red-shift of about 6 GHz for HFAP, provides insights into the parameters χ and ξ . This suggests that both acoustic components could originate from two distinct branches of acoustic phonons (refer to Supplementary Sec. VII). From the analysis (refer to Supplementary Sec. VII and Fig. S17 and S18), the values of χ and ξ are found to be $\sim 1.7 \text{ mHz } m^2/A^2s$ and $10.2 \text{ THz } m^2/A^2s$, respectively.

Also note that the distortion field Q is modified to $\bar{Q}_j = Q_j - \frac{\gamma}{2\xi}$ by spin-phonon coupling. After the onset of magnetic order below T_{3D} , the amplitude can become negative for large $\frac{\gamma}{2\xi}$, leading to a phase inversion of the distortions [28]. Above T_{3D} , even though there is no finite magnetisation M , Q can still couple with the spin fluctuations $\langle(\vec{S}_j \cdot \vec{S}_{j+1})^2\rangle - \langle\vec{S}_j \cdot \vec{S}_{j+1}\rangle^2$, again leading to a reduced amplitude.

Also, above T_{3D} the frequency of both HFAP as well as the LFAP (although weakly) exhibits a decreasing trend with increasing temperature as expected from anharmonic phonon decay [23, 24, 25, 26]. The temperature-dependent frequency variation is modeled using the anharmonic phonon decay model and depicted as black dashed lines in Fig. 3 (details of the model are available in Supplementary Sec. V). Importantly, the frequency variation of the LFAP with increasing temperature is less pronounced compared to the HFAP, indicating weaker anharmonic coupling in the LFAP. Further discussion on the frequency shift and lifetime of both LFAP and HFAP can be found in Supplementary Sec. V.

Conclusions

In conclusion, our comprehensive non-degenerate pump-probe experiments combined with a phenomenological model provide a profound understanding of the intricate interplay between spin, charge and lattice degrees of freedom in the 2D Heisenberg ferromagnet CrSiTe₃. We unveil the distinct stages of magnetic dimensional crossover and their impact on both ultrafast carrier dynamics and acoustic phonons. Notably, our findings confirm the crucial role of interlayer spin-spin interactions in stabilizing long-range magnetic order at high temperatures. Furthermore, we shed light on the specific influence of different magnetic phases on the acoustic strain spectrum. Remarkably, the long-range magnetic order fluctuations renormalize the frequency of high-frequency acoustic strain part, while also gapping out the low-frequency part. These intricate observations have provided valuable insights into the microscopic coupling between carriers, spin and lattice degrees of freedom, that are vital in the design of spin-based optoelectronic devices based on 2D ferromagnetic materials like CrSiTe₃.

Methods

Sample growth and characterization: CrSiTe₃ single crystals were synthesized via a self-flux technique. High-purity starting materials, Cr (99.999% from Alfa Aesar), Si (99.999% from Alfa Aesar), and Te (99.9999% from Alfa Aesar), were combined in a 1:2:6 molar ratio and placed within a 10 ml alumina crucible. A second crucible with quartz wool was positioned on top of the growth crucible, and the setup was enclosed in a quartz tube filled with high-purity argon gas. The sealed ampoule underwent gradual heating to 1100 °C over 7 hours, followed by a 15-hour hold at 1100 °C, and finally cooling to 700 °C at a rate of 3.2 °C/h. Upon reaching 700 °C, excess flux was removed from the crystals by centrifuge technique.

X-ray diffraction (XRD) and energy-dispersive X-ray analysis (EDAX) were employed to analyse the structure and chemical composition of CrSiTe₃ crystal (Refer Fig. S1 and Tab. TS1 of

the Supplementary). From XRD it is confirmed that CrSiTe₃ crystallizes to R3, space group 148. Temperature dependent powder X-ray diffraction measurements were performed on crushed single crystals using a Rigaku X-ray diffractometer (Smart Lab, 9kW) with Cu K alpha radiation ($\lambda = 1.540$ Angstrom) over a temperature range of 10-300 K (refer to Supplementary Fig. S2). Raman spectroscopy (Horiba jobin Yvon - HR800, 488 nm excitation) was used to characterize the typical Raman modes of CrSiTe₃ single crystal (refer to Supplementary Fig. S3). Temperature dependence of the magnetization (M) in field-cooled and zero-field-cooled modes under a magnetic field of 1 kOe applied along the c-axis (refer to Supplementary Fig. S4).

Pump Probe Spectroscopy: Temperature dependent time-resolved non-degenerate transient reflection experiments were used to examine the photoexcited carrier dynamics of CrSiTe₃ single crystal. The pump-probe setup is set in the reflection geometry. The beam from the Amplifier laser (Spectra Physics Solstice Ace, 800 nm, 1 kHz, 50 fs, 5mJ) was split in two parts. One part of the beam is fed to Optical Parametric Amplifier (Light Conversion TOPAS Prime) to get 650 nm output. The other beam of 800 nm is used for probing the sample. Both the beams are time-delay matched using a retro-reflector on the 600 ps delay stage. The pump beam is modulated at 333 Hz using a mechanical chopper. The change in reflectivity with respect to with and without pump is detected using a balanced photo diode. The sample was cooled using a flow type cryostat (Oxford Instruments) with liquid Helium and hence the sample surface remained in the inert atmosphere all throughout the measurements. The measured full width half maximum spot size of pump and probe were $\sim 600 \mu\text{m}$ and $\sim 400 \mu\text{m}$, respectively. The pump and probe fluences were kept at 1.77 mJ/cm^2 and $133 \mu\text{J/cm}^2$ at all the temperatures.

References

- [1] Burch, K. S., Mandrus, D., & Park, J. G. Magnetism in two-dimensional van der Waals materials. *Nature*, 563, 47-52 (2018).
- [2] Li, H., Ruan, S., & Zeng, Y. J. Intrinsic van der Waals magnetic materials from bulk to the 2D limit: new frontiers of spintronics. *Adv. Mater.* 31, 1900065 (2019).
- [3] Huang, B., et al. Layer-dependent ferromagnetism in a van der Waals crystal down to the monolayer limit. *Nature*, 546, 270-273 (2017).
- [4] Gong, C., et al. Discovery of intrinsic ferromagnetism in two-dimensional van der Waals crystals. *Nature*, 546, 265-269 (2017).
- [5] Girovsky, J., et al. Long-range ferrimagnetic order in a two-dimensional supramolecular Kondo lattice. *Nat. Commun.* 8, 15388 (2017).
- [6] Mermin, N. D., & Wagner, H. Absence of ferromagnetism or antiferromagnetism in one-or two-dimensional isotropic Heisenberg models. *Phys. Rev. Lett.* 17, 1133 (1966).
- [7] Hohenberg, P. C. Existence of Long-Range Order in One and Two Dimensions. *Phys. Rev.* 158, 383-386 (1967).

- [8] Ron, A., et al. Dimensional crossover in a layered ferromagnet detected by spin correlation driven distortions. *Nat. Commun.* 10, 1654 (2019).
- [9] Casto, L. D., et al. Strong spin-lattice coupling in CrSiTe₃. *APL Mater.* 3 (2015).
- [10] Milosavljević, A., et al. Evidence of spin-phonon coupling in CrSiTe₃. *Phys. Rev. B*, 98, 104306 (2018).
- [11] Ron, A., et al. Ultrafast enhancement of ferromagnetic spin exchange induced by ligand-to-metal charge transfer. *Phys. Rev. Lett.* 125, 197203 (2020).
- [12] Thomsen, C., et al. Surface generation and detection of phonons by picosecond light pulses. *Phys. Rev. B*, 34 4129 (1986).
- [13] Wu, S., et al. Femtosecond optical generation and detection of coherent acoustic phonons in GaN single crystals. *Phys. Rev. B*, 76, 085210 (2007).
- [14] von Reppert, Alexander, et al. Unconventional picosecond strain pulses resulting from the saturation of magnetic stress within a photoexcited rare earth layer. *Struct. Dyn.* 7 (2020).
- [15] Mattern, Maximilian, et al. Towards shaping picosecond strain pulses via magnetostrictive transducers. *Photoacoustics* 30, 100463 (2023).
- [16] Lovinger, D. J., et al. Magnetoelastic coupling to coherent acoustic phonon modes in the ferrimagnetic insulator GdTlO₃. *Phys. Rev. B*, 102, 085138 (2020).
- [17] Fu, Jianhui, et al. Strain propagation in layered two-dimensional halide perovskites. *Sci. Adv.* 8, eabq1971 (2022).
- [18] Williams, Travis J., et al. Magnetic correlations in the quasi-two-dimensional semiconducting ferromagnet CrSiTe₃. *Phys. Rev. B*, 92, 144404 (2015).
- [19] Guo, J., Liang, W., & Luo, S. N. Anomalous Hot Carrier Decay in Ferromagnetic Cr₂Ge₂Te₂ via Spin–Phonon Coupling. *J. Phys. Chem. Lett.* 11, 9351-9357. (2020).
- [20] Liu, Junfeng, et al. Electron Density Changes and Ultrafast Carrier Dynamics of the Antiferromagnetic Semiconductor MnPS₃ through Magnetic Phase Transition. *Inorg. Chem.* 61, 18380-18389 (2022).
- [21] Sutcliffe, Erica, et al. Transient magneto-optical spectrum of photoexcited electrons in the van der Waals ferromagnet Cr₂Ge₂Te₂. *Phys. Rev. B*, 107, 174432 (2023).
- [22] Beaurepaire, E., Merle, J. C., Daunois, A., & Bigot, J. Y. Ultrafast spin dynamics in ferromagnetic nickel. *Phys. Rev. Lett.* 76, 4250 (1996).
- [23] Lichtenberg, Tom, et al. Anisotropic laser-pulse-induced magnetization dynamics in van der Waals magnet Fe₃GeTe₂. *2D Mater.* 10, 015008 (2022).

- [24] Li, Ning, et al. Abnormal Hot Carrier Decay via Spin–Phonon Coupling in Intercalated van der Waals Ferromagnetic $\text{Fe}_{1/3}\text{TaS}_2$. *Nano Lett.* 22, 3849-3855 (2022).
- [25] Yan, X., & He, J. Extending Carrier Lifetime of Antiferromagnetic LaFeO_3 Perovskite by Regulating Magnetic Ordering: Time-Domain Ab Initio Analysis. *J. Phys. Chem. Lett.* 14, 5867-5875 (2023).
- [26] Schmising, C. V. Korff, et al. Ultrafast magnetostriction and phonon-mediated stress in a photoexcited ferromagnet. *Phys. Rev. B*, 78, 060404 (2008).
- [27] von Reppert, A., et al. Spin stress contribution to the lattice dynamics of FePt. *Sci. Adv.* 6, eaba1142 (2020).
- [28] Ergeçen, Emre, et al. Coherent detection of hidden spin–lattice coupling in a van der Waals antiferromagnet. *PNAS*, 120, e2208968120 (2023).
- [29] Orbach, R., & Vredevoe, L. A. The Attenuation of high frequency phonons at low temperatures. *Phys. Phys. Fiz.* 1, 91 (1964).
- [30] Klemens, P. G. Decay of high-frequency longitudinal phonons. *J. Appl. Phys.* 38, 4573-4576 (1967).
- [31] Baumgartner, R., Engelhardt, M., & Renk, K. F. Spontaneous Decay of High-Frequency Acoustic Phonons in CaF_2 . *Phys. Rev. Lett.* 47, 1403 (1981).
- [32] Tamura, S. I. Spontaneous decay rates of LA phonons in quasi-isotropic solids. *Phys. Rev. B*, 31, 2574 (1985).

Supplementary information

Additional discussion on sample characterization (Supplementary Section *I*), data fitting of pump probe dynamics and extracted parameters and their temperature dependence (Supplementary Sections *II* and *III*), origin of picosecond strain pulses and their characteristics in time and frequency domain (Supplementary Sections *IV* and *V*), details of theoretical model and the extraction of coupling constants (Supplementary Sections *VI* and *VII*) and details of data fitting (Supplementary Section *VIII*).

Acknowledgments

The authors thank the Ministry of Education (MoE), Government of India for funding and IISER Kolkata for the infrastructural support to carry out the research. ANM, and SM thank IISER Kolkata and DST-INSPIRE respectively for their research fellowship. The authors thank Poulami Ghosh and Pediseti Venkatesh for designing the essential schematics. SL thanks the SERB, Govt. of India for funding through MATRICS grant MTR/2021/000141 and Core Research Grant CRG/2021/000852. N. K thanks the SERB, Govt. of India for funding through Core Research Grant CRG/2021/004885.

Authors' contributions

A.N.M and N.K. conceived the idea, the project and the analysis. A.N.M, S.M. and A.P. performed the time-resolved non-degenerate pump probe measurements assisted by S.G.P and N.K. T.S and S.P grew the crystals and measured the temperature dependent magnetization. A.M and S.L developed the theoretical model. A.N.M, and N.K. interpreted the results. A. N.M, S.M., A.M., A.P, S.G.P, S.L, and N. K were involved in the writing of the manuscript. All the authors agree to the content of the final version.

I Sample characterization

I.a Single crystal XRD, Energy-dispersive X-ray analysis

CrSiTe_3 is a two-dimensional ferromagnetic semiconductor that crystallizes in a rhombohedral structure. The crystal structure consists of three CrSiTe_3 layers stacked in an ABC sequence, with alternating Te-Cr-Te and Te-Si-Te layers. Within each layer, the Cr atoms form a honeycomb lattice, which is offset from the honeycomb lattices of the adjacent layers [1]. The Cr^{3+} ions are situated at the center of a distorted octahedron of six Te atoms (ligand), while the two Si atoms are paired and located between two opposing Te triangles. Here, X-ray diffraction (XRD) and energy-dispersive X-ray analysis (EDAX) is used to determine the structure and chemical composition of CrSiTe_3 crystal used in this measurement. Figure S1 shows the XRD data for a single crystal of CrSiTe_3 at room temperature. The peaks in the XRD data match those reported in the literature [1, 2, 3], confirming that the crystal is of high quality and is oriented along the c-axis.

Table TS1 shows the chemical composition of the single crystal CrSiTe_3 .

Table TS1: Chemical composition of CrSiTe_3 : Exact chemical composition of CrSiTe_3 single crystal obtained from EDAX is shown here.

Cr (atomic %)	Si (atomic %)	Te (atomic %)
17.49	22.47	60.03
17.49	22.17	60.03
18.06	22.03	59.90
19.14	22.55	58.41
Exact composition : $\text{Cr}_{0.9}\text{Si}_{1.1}\text{Te}_{2.9}$		

I.b Temperature dependent X-ray powder diffraction.

To investigate any changes in the crystal structure, temperature-dependent powder X-ray diffraction (XRD) measurements were performed on crushed single crystals using a Rigaku Smart Lab 9kW diffractometer with Cu $K\alpha$ radiation (wavelength $\lambda = 1.540$) over a temperature range of 10-300 K. Supplementary Fig. S2. shows the temperature-dependent powder XRD data. No significant peak shifts or broadening were observed across the entire temperature range, confirming the absence of any structural phase transition.

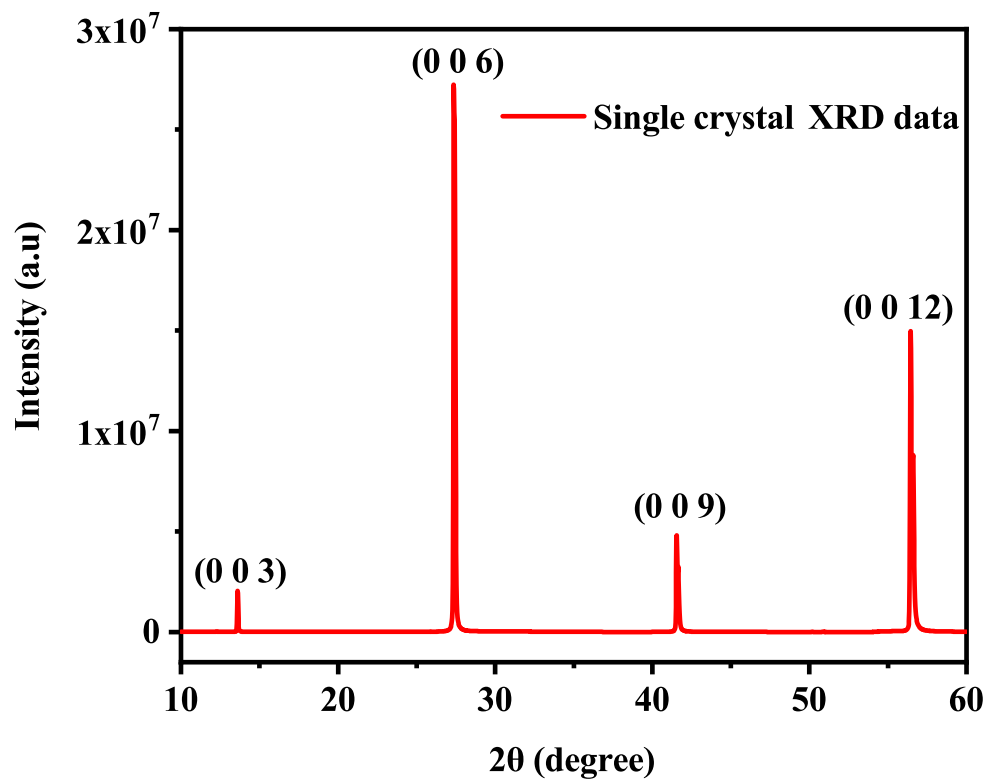


FIG S1: X-ray diffraction spectrum of CrSiTe₃: Room temperature X-ray diffraction (XRD) pattern of a single crystal of CrSiTe₃, showing peaks corresponding to the (003), (006), (009), and (0012) planes. The peaks are consistent with the literature [1, 2, 3], indicating the high quality of the crystal.

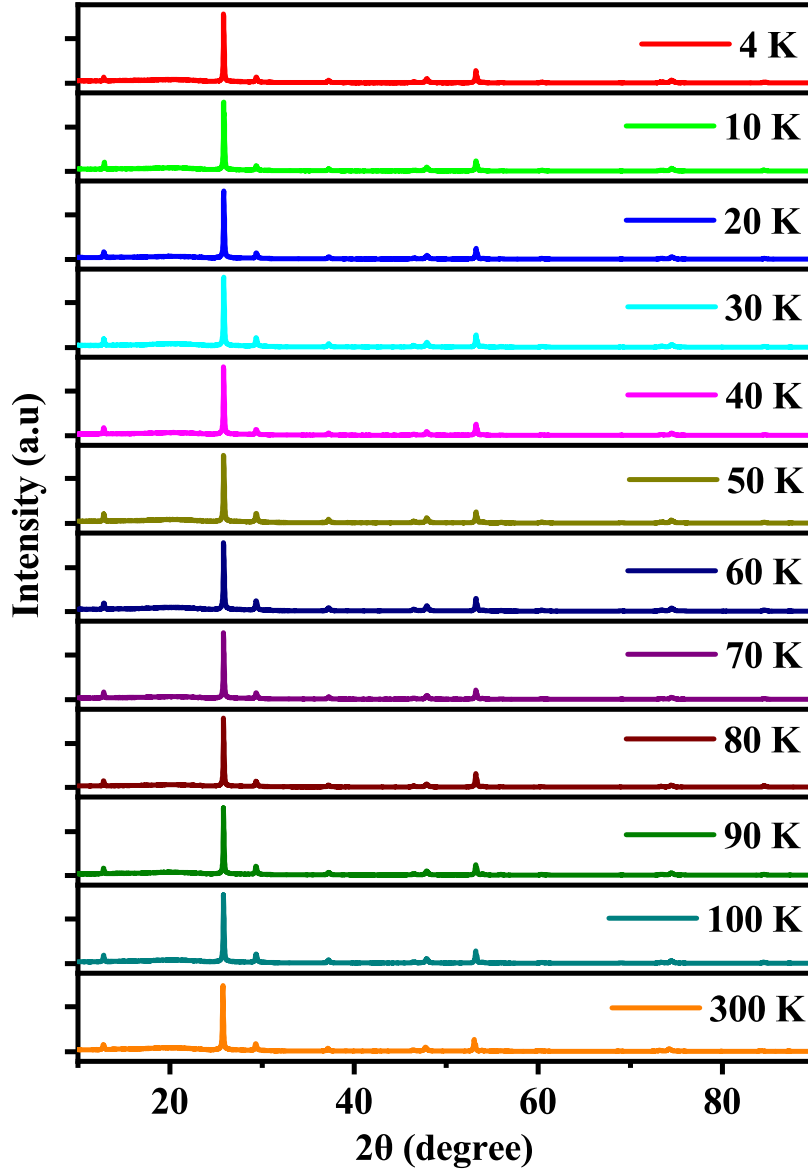


FIG S2: Temperature dependent powder x-ray diffraction: Temperature-dependent powder X-ray diffraction (XRD) spectra of CrSiTe₃ at various temperatures from 4 K to 300 K. No significant peak shifts or broadening were observed, indicating the absence of a structural phase transition.

Table TS2: Raman spectroscopy of CrSiTe₃: The extracted parameters from the multi-Lorentzian fit to the Raman spectrum are tabulated here

Raman mode	Wave number (cm ⁻¹)	FWHM (cm ⁻¹)
A _g ¹	84.0 ± 0.6	3.0 ± 0.9
E _g ¹	89.5 ± 0.5	3.2 ± 1.0
E _g ³	117.4 ± 0.03	2.2 ± 0.1
A _g ³	146.9 ± 0.07	2.6 ± 0.2

I.c Raman Spectroscopy of CrSiTe₃ single crystal.

Raman spectroscopy (Horiba Jobin Yvon - HR800, 488 nm excitation) was used to record the Raman spectrum from the sample. Figure S3 shows the Raman spectrum of bulk CrSiTe₃ single crystals. Multi-Lorentzian fitting of the Raman spectrum revealed four distinct peaks at 84 cm⁻¹, 89.5 cm⁻¹, 117.45 cm⁻¹ and 146.9 cm⁻¹, which are assigned to the A_g¹, E_g¹, E_g³ and A_g³ modes, respectively. Observed peak positions and full width half maxima (see Tab. TS2) values match those reported in prior work [2, 4].

I.d Magnetization of CrSiTe₃.

Figure S4 (a) shows the temperature dependence of the magnetization (M) in field-cooled (red line) and zero-field-cooled (black line) modes under a magnetic field of 1 kOe applied along the c-axis. The temperature dependence of M reveals a ferromagnetic transition at a Curie temperature (T_c) of 33 K (refer Fig 2(b) of the main manuscript). Figure S4(b) shows the magnetization as a function of magnetic field (H) along the c-axis at 3 K (black) and 300 K (red), respectively [1].

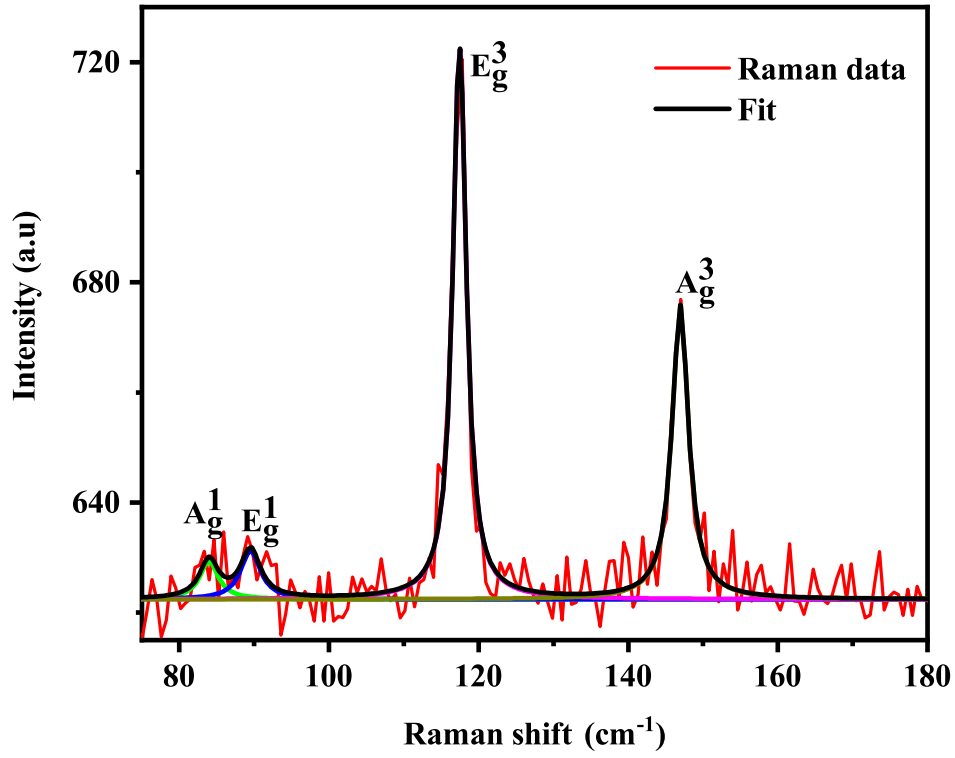


FIG S3: Room temperature Raman Spectroscopy: Raman data (red lines) of bulk CrSiTe_3 along with its fit. The corresponding multi-Lorentzian fit shown in the black line. Five Lorentzian functions, represented individually by the green, blue, magenta and dark yellow solid lines.

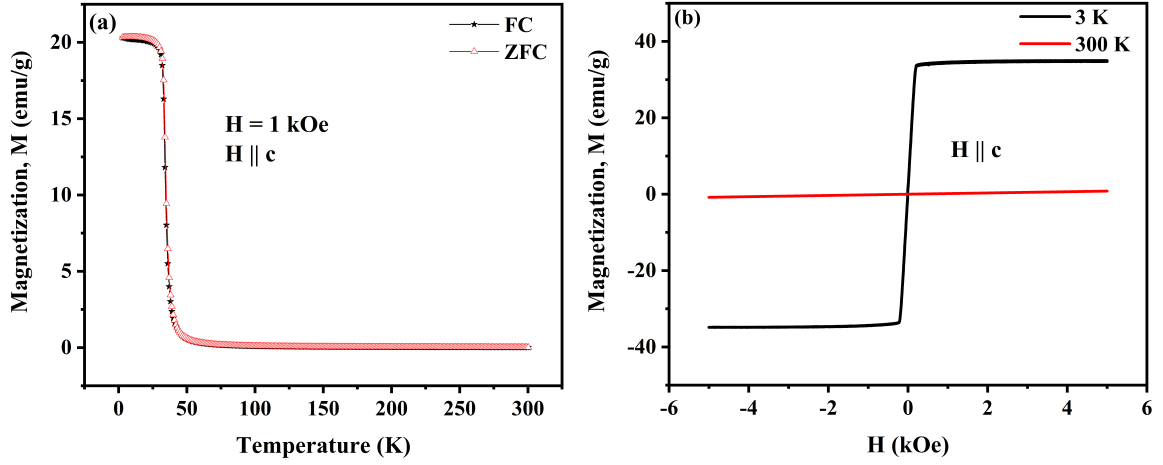


FIG S4: Magnetization of CrSiTe₃ as a function of temperature and magnetic field: a) Magnetization (M) as a function of temperature measured under a magnetic field of 1 kOe applied along the c-axis, in field-cooled (black line + closed star) and zero-field-cooled (red line + open triangle) modes, respectively. (b) Magnetization as a function of magnetic field (H) along the c-axis, measured at 3 K (black solid line) and 300 K (red solid line), respectively.

II Pump probe dynamics and data analysis.

Figure S5 (a) shows a 2D false-color map of the temperature evolution of the photoinduced transient differential reflectivity (DR) data of a single crystal of CrSiTe₃ pumped at 650 nm with a fluence of 1.77 mJ/cm². As indicated by the black arrow in Fig. S5(a), a noticeable change in the raw DR/R data can be seen across the Curie temperature (T_c). This change indicates that the transient reflectivity data is indeed affected by the magnetic phase transition, which is the first signature of magneto-elastic coupling in CrSiTe₃. For clarity, the data at 4 K and 300 K are shown in Fig. S5(b,c). The photoinduced transient reflectivity data has three main features at all temperatures: a positive peak at zero pump-probe delay, followed by strain-induced oscillation on top of the exponentially decaying electronic part.

The DR response upon pump excitation in semiconductors is caused by the change of the complex refractive index of the sample associated with optical transitions[5, 6] and results in the positive sign. CrSiTe₃ has an indirect band gap of 0.4 eV and a direct band gap of 1.2 eV. The valence band of CrSiTe₃ is primarily composed of Te 5p levels and the conduction band is mainly composed of Cr 3d levels (refer to Fig. S6) [7, 8]. The central photon energy of the pump (~ 1.9 eV) and probe (~ 1.55 eV) pulses in our experiment is within the direct band gap of CrSiTe₃. As a result, both the pump and the probe pulses can excite electrons from the Te p levels to the Cr d levels [16]. This leads to a reduction in the absorption of the probe pulse in the presence of a strong pump pulse, which is known as the state filling effect.

To understand the carrier dynamics in CrSiTe₃, the exponentially decaying electronic background of the DR data was fitted with a multi-exponential decay function. At all the temperatures,

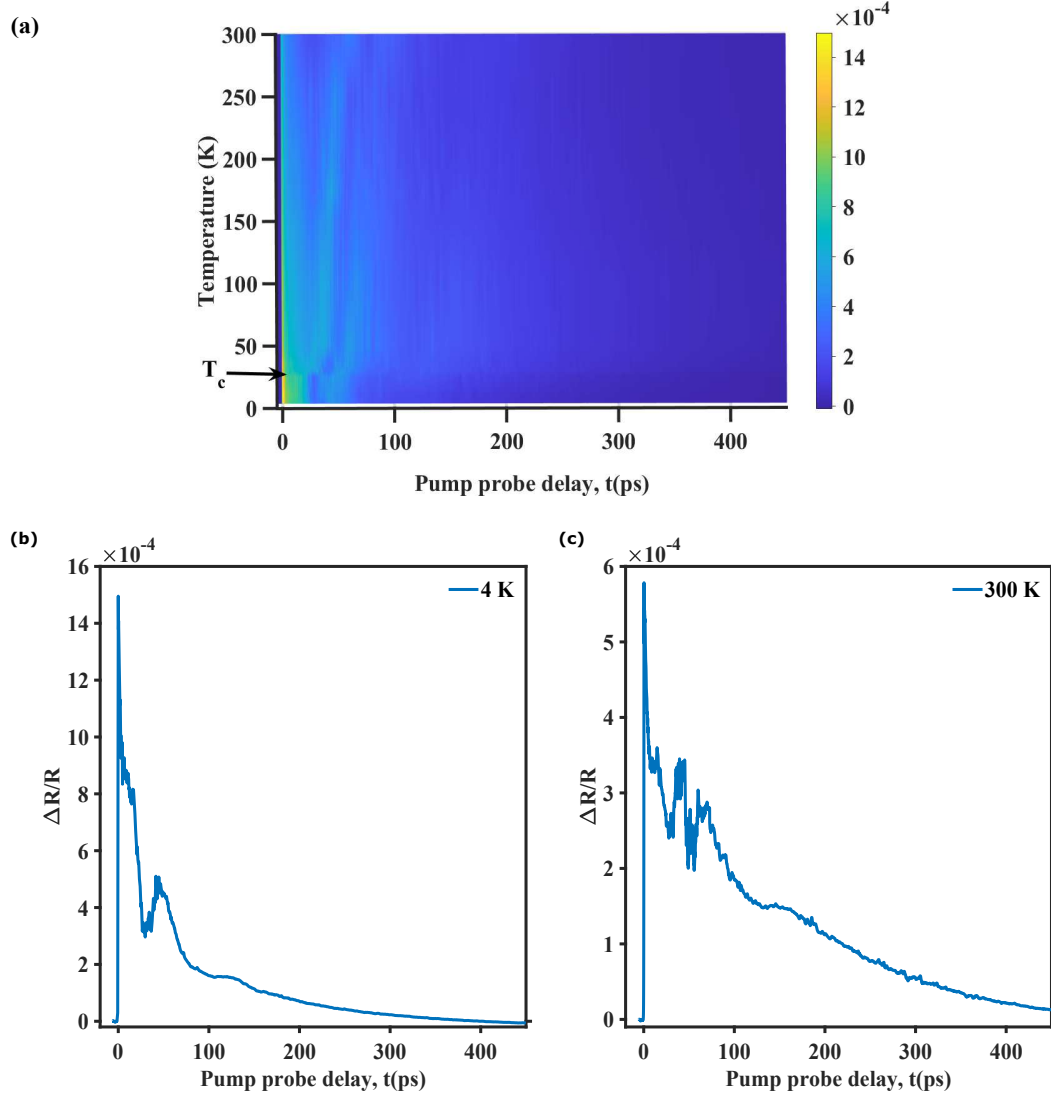


FIG S5: Temperature evolution of pump-probe dynamics: (a) Two-dimensional color map of the temperature evolution of the transient differential reflectivity (DR) data of CrSiTe₃, shown up to 450 ps of the pump-probe delay at all measured temperatures from 4 K to 300 K. The black solid arrow indicates the Curie temperature (T_c). (b) and (c) shows the raw DR data at 4 K and 300 K, respectively.

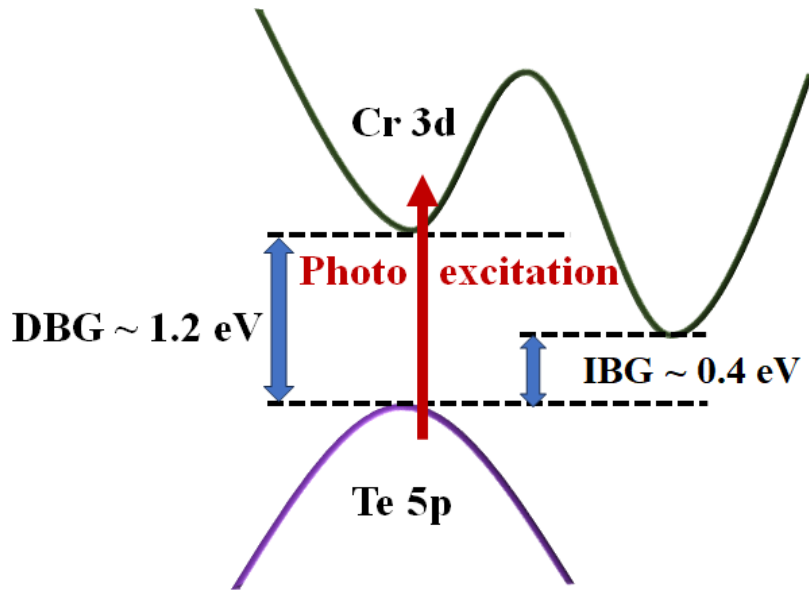


FIG S6: Schematic band diagram of CrSiTe₃: The valance band is mainly composed of Te 5p levels and conduction band is mainly composed of Cr 3d levels. The direct (DBG) and in-direct band gap (IBG) is ~ 1.2 eV and ~ 0.4 eV, respectively. Photo-excitation using 1.9 eV is indicated in solid red arrow.

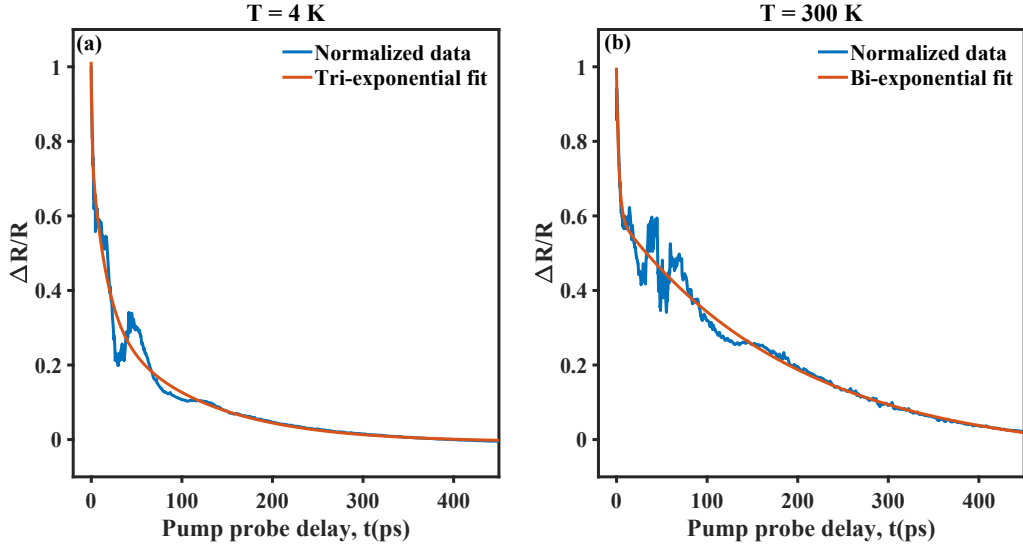


FIG S7: Raw transient differential reflectivity data and its multi-exponential fit: Normalized transient differential reflectivity data (blue solid line) of CrSiTe₃ single crystal and their fit to tri exponential (orange solid line) and Bi-exponential functions (orange solid line) at (a) 4 K and (b) 300K, respectively presented until the pump probe delay time (t) of 450 ps. The data is normalized with respect to its peak value.

the DR data was normalized to its peak value and cut at 0 ps and fitted with a multi-exponential function up to the pump probe delay of 450 ps to extract the relaxation timescales and the decay coefficients. Interestingly, below 35 K (including 35 K), the data could be successfully fitted to a minimum sum of three exponential functions (shown in Fig. S7 (a)) with a constant background A_0 , given by

$$\Delta R/R = \sum_{i=1}^3 A_i \exp(-t/\tau_i) + A_0 \quad (6)$$

Whereas, above 35 K (from 50K data) the data could be successfully fitted to minimum sum of bi-exponential functions (shown in Fig. S7 (b)) with a constant background,

$$\Delta R/R = \sum_{i=1}^2 A_i \exp(-t/\tau_i) + A_0 \quad (7)$$

where A 's are the decay coefficients and τ 's are the relaxation timescales.

To justify why at least three exponentials are needed to fit the DR data below 35 K, the data at 35 K was fit with both two- and three-exponential functions (Fig. S8). From the figure S8 (a) and its inset, it is clear graphically that the tri-exponential function (black solid line) fits the data well, while the bi-exponential function (yellow solid line) deviates from the experimental DR data (blue solid line). Therefore, at least three exponentials are needed to fit the DR data below 35 K. At 50 K

and higher temperatures, the data could be fitted with both two- and three-exponential functions (refer to Fig. S8 (b) and (c), where the data and the fit at 50 K and 100 K are shown for clarity). The fits are similar in both cases (refer to inset of Fig. S8 b and c), and the goodness of fit (R^2 value) is nearly identical: 0.977 and 0.978 for bi- and tri-exponential fits at 50 K, and 0.974 for both bi- and tri-exponential fits at 100 K. Therefore, we prefer to fit the data at and above 50 K with two exponentials, since it has minimum number of exponentials.

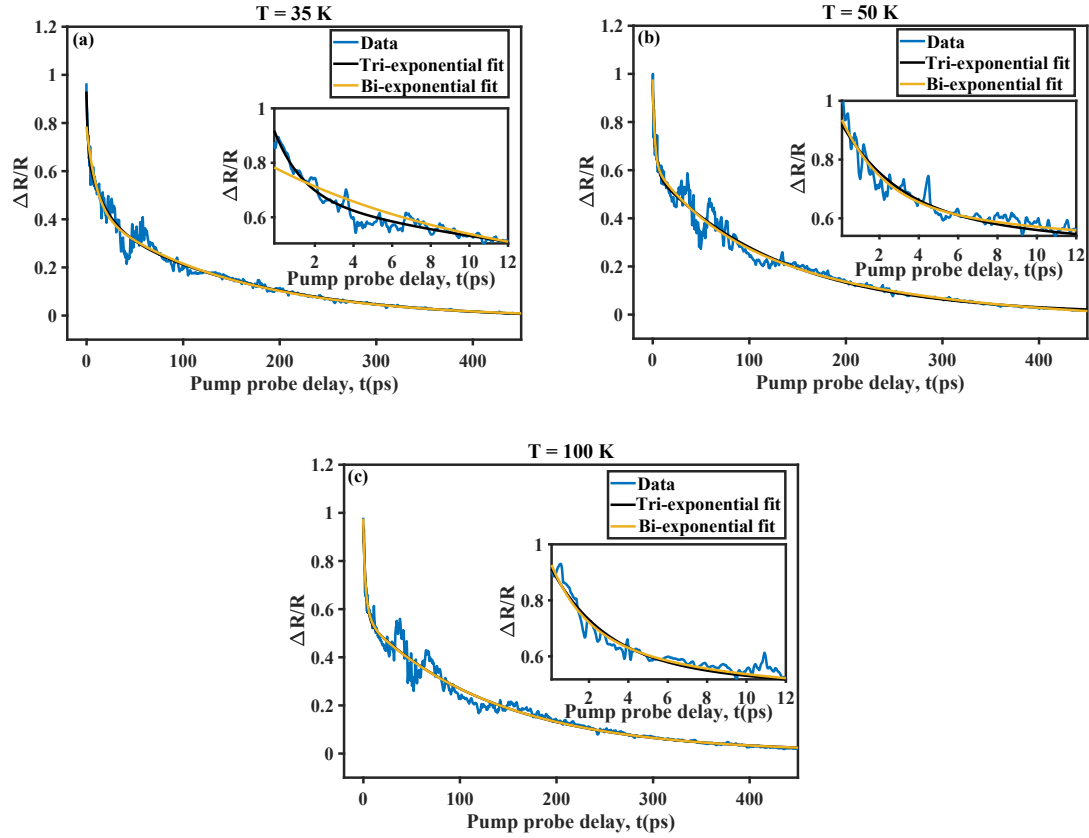


FIG S8: Comparison of Bi and Tri-exponential fits to the DR data: The transient differential reflectivity data (blue solid line) normalized with respect to its peak value and cut at 0 ps of the pump probe delay is fitted with both minimum sum of two exponentials (yellow solid line) and minimum sum of three exponential functions (black solid line) for comparison at (a) 35 K, (b) 50 K and (c) 100 K respectively. For clarity, the data and the respective fits are shown up to 12 ps of the pump probe delay time in the insets of each figures.

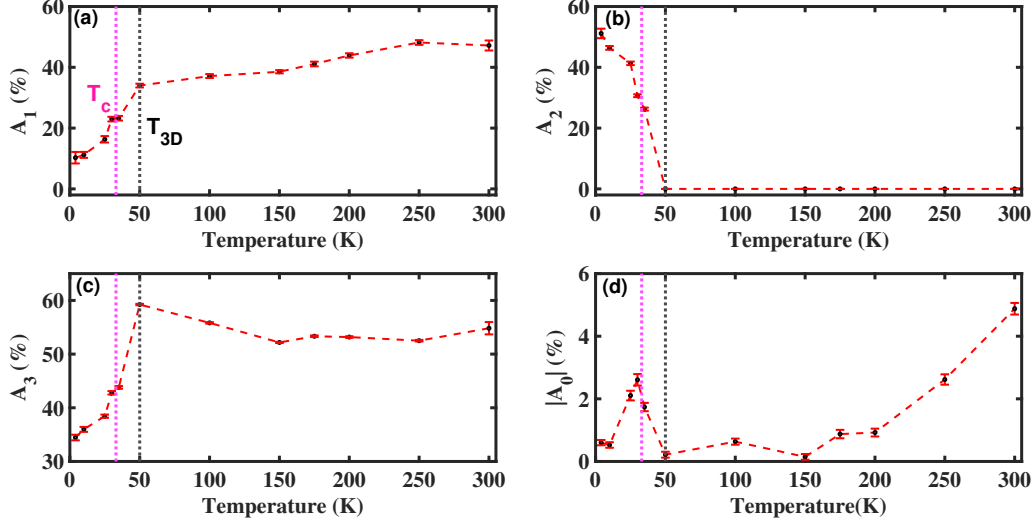


FIG S9: Temperature dependent decay coefficients: The variation of the decay coefficients (a) A_1 , (b) A_2 , (c) A_3 and (d) absolute value of A_0 as a function of the temperature. The error bars are determined using orthogonal distance regression (ODR) approach. The red dashed lines are guide to eye. The magenta and black vertical dotted line indicates the Curie temperature (T_c) and the temperature (T_{3D}) at which the onset of LRMO fluctuations begin.

III Decay coefficients and their temperature dependence.

The relaxation timescales and decay coefficients of the transient differential reflectivity (DR) data are extracted from a multi-exponential fit. The relaxation timescales and their temperature dependence are discussed in the main manuscript (refer to Fig. 2 (b) of the manuscript), while the decay coefficients and their temperature dependence are shown in Fig. S9. A_1 varies from $\sim 15\%$ to $\sim 40\%$ in the temperature range 4 K to 50 K. Through-out this temperature range A_1 increases with the increasing temperature. Also, the relaxation timescale, τ_1 (1-3 ps) associated with this coefficient suggest this process is associated with the electron-lattice - spin thermalization (see main manuscript) [6]. A_2 is only present below 50 K and decreases from $\sim 50\%$ to $\sim 20\%$ (from 4 K to 35 K) as the temperature increases. Therefore this processes is attributed to the interaction of lattice with interlayer spin-spin fluctuations. A_3 increases from $\sim 20\%$ to $\sim 60\%$ as the temperature increases from 4 K to 50 K, and then remains constant with the temperature above 50 K. This process is associated with the lattice interaction with the intralayer spin-spin fluctuations. A_0 is the coefficient associated with the long decay process and it varies from ~ 2 to $\sim 4\%$. The similar relaxation timescales and decay coefficients have been seen in the nano-sheet of CrSiTe₃ [6]. These results suggest that all the decay coefficients undergo a drastic change at the T_{3D} temperature, which is the onset of the long-range magnetic order (LRMO) fluctuations.

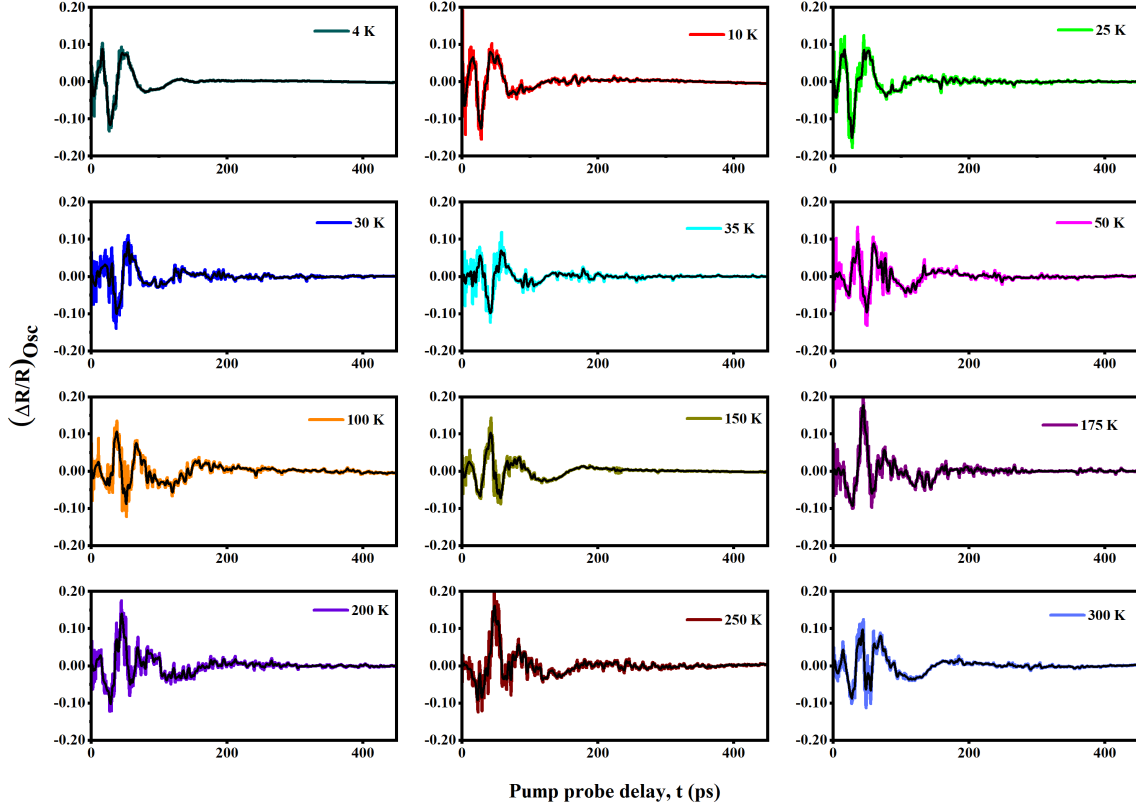


FIG S10: Strain pulses at various temperatures: This figure shows strain pulses extracted from transient differential reflectivity data for CrSiTe_3 at various temperatures, represented by different colored solid lines. The smoothened data at each temperature is shown in the black solid lines

IV Picosecond strain pulse: Origin of strain pulse and the effect of magnetic ordering on the strain pulse.

The interesting feature of the DR data is the strain pulse. We extracted the oscillatory component by subtracting the multi-exponential fits at each temperature. Figure S10 shows the temperature evolution of DR oscillations for all temperatures and pump-probe delay times up to ~ 450 ps. The variation of the strain pulse as a function of temperature is discussed in the main manuscript, therefore this section focuses on the origin of the strain pulse. For clarity, smoothened data of strain pulse at various temperatures is shown the Fig 2 (d) of the main manuscript. The smoothening is done by using the smoothening function ‘Loess’ with the x-axis increment 0.01 using MATLAB software. Figure S11 (a) here compares the raw strain pulse data (various colored lines) and its smoothened data (black line) in the time domain. The corresponding FFT spectra of raw and smoothened data are shown in Fig S11 (b). It is important to note that the smoothening does not alter the data, which is evident from the FFT spectrum of both raw and smoothened data shown in Fig. S11 (b).

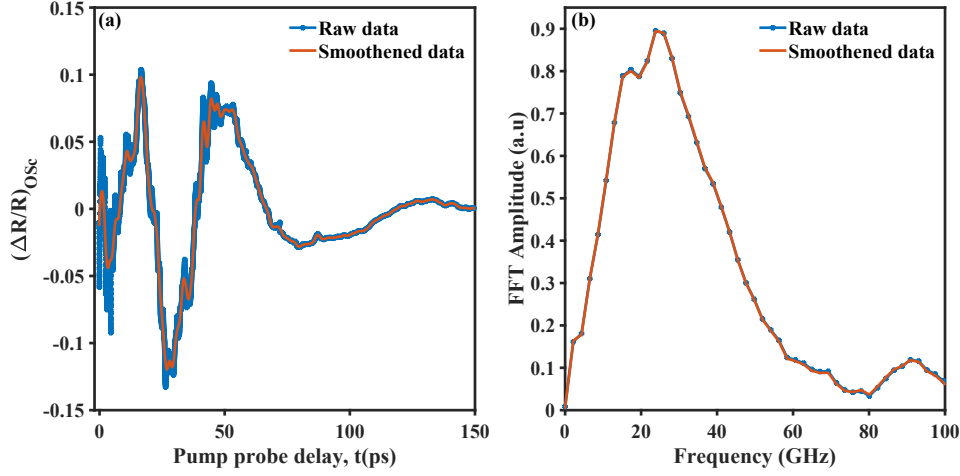


FIG S11: Data processing: (a) Time-domain strain pulse of CrSiTe₃ at 4K. The raw data is shown in blue squares with line, and the smoothed data is shown in orange solid line. The corresponding FFT spectra are shown in panel (b)

The strain pulses in Fig. S11 (a) resemble a single-cycle pulse rather than sinusoidal oscillations. These are caused by lattice strain which in turn is associated with lattice stress. Several mechanisms can contribute to lattice stress in materials, including thermal expansion (TE) stress [10], deformation potential (DP) interaction[11], inverse piezoelectric interaction[12], and magnetic stresses[13, 14, 15]. TE stress arises from the transfer of excess energy from photoexcited carriers to the lattice via electron-phonon interaction as they relax to the band edge, causing a rapid increase in lattice temperature. DP interaction occurs when photo-excitation of electrons from the valence band to the conduction band disrupts lattice equilibrium, leading to lattice deformation. This deformation alters the semiconductor band structure and induces electronic stress associated with free carriers in conduction band. Inverse piezoelectric interaction arises when photoexcited charge carriers screen the intrinsic built-in electric field in non-centro-symmetric materials, modifying the lattice equilibrium state via the inverse piezoelectric effect and generating inverse piezoelectric stress (IP). Since CrSiTe₃ is a centro-symmetric crystal, the piezoelectric effect is negligible. The presence of electron-phonon thermalization (decay coefficient $A_1 \sim 40\%$) in the electronic background of DR and at typical photoexcited carrier density $N \sim 4.2 \times 10^{20} \text{ cm}^{-3}$ (estimated using $N = \frac{F\alpha R}{E}$, where F is the fluence in mJ/cm^2 , α is the absorption coefficient in cm^{-1} , R is the reflectivity, and E is the pump photon energy), both TE and DP processes dominantly contribute to the strain pulse in this material in the paramagnetic phase. In the ferromagnetic compound CrSiTe₃, the magnetic order arises from super-exchange interactions between chromium (Cr) metal atoms mediated by tellurium (Te) ligands. A recent study[16] suggests that photo-excitation-induced charge transfer from ligands to metal ions can significantly increase the super-exchange interaction energy. This strengthened interaction, in turn, will introduce additional magnetic stress through the magnetostrictive mechanism in the ferromagnetic state. Therefore in the ferromagnetic phase, the strain arise from all three

processes, which is given by[15]

$$\eta_{Total}(x,t) = \eta_{TE}(x,t) + \eta_{DP}(x,t) + \eta_{Magnetic}(x,t) \quad (8)$$

where $\eta_{TE}(x,t)$, $\eta_{DP}(x,t)$, $\eta_{Magnetic}(x,t)$ are the strain due to TE, DP and Magnetic origins.

Magnetic materials often thus exhibit a competition between contrasting forces: expansive stresses arising from elastic processes (TE and DP) and a contractive stress induced by magnetic order. This interplay leads to the emergence of intricate spatio-temporal strain pulses, a phenomenon observed in materials like dysprosium [14, 15], FePt thin films[17, 18], and SrRuO₃ nano-layers in a SrRuO₃/SrTiO₃ super-lattices [13]. Alexander von Reppert et al.[14] have explained this complex interaction by modeling the spin system as an energy reservoir with a saturation limit. This reservoir generates substantial contractive stress on ultrafast timescales, explaining the observed intricate strain response. Additionally, their model enabled the estimation of the time- and space-dependent magnetic stress.

The interplay between various strain generation processes enable us to capture the each distinct step of the magnetic dimensional crossover using picosecond strain pulses. The main manuscript discusses the effect of magnetic dimensional crossover on the strain pulses. For example, Fig. S12 shows the strain pulse in the ferromagnetic phase (4 K) and in the paramagnetic phase (150 K). For clarity, only data at two temperatures are shown here. As evident from Fig. S12, the strain pulse at 4 K is inverted compared to the strain pulse at 150 K. This indicates that the contractive magnetic stress in the FM phase dominates over the expansive elastic stress.

To quantify the interaction between the processes, we calculated the peak-to-peak difference (ΔP) and the area difference (ΔA) of the positive and negative portions of the central part of the strain pulses. ΔP was obtained by summing the positive peak value (P_p) and the negative peak value (P_n) of the central peak. To account for potential fluctuations in the peak values, we also calculated ΔA by adding the positive area (A_p) and negative area (A_n) of the central part of the strain pulse. The extraction procedure for both ΔP and ΔA is illustrated in Fig. S13 for data at 50K. The same procedure was repeated for all temperatures for consistency.

V Picosecond strain pulse: frequency domain spectrum.

V.a Fast Fourier Transform (FFT)

The frequency domain spectrum of the strain pulse is obtained using the fast Fourier transform (FFT). The FFT of the time domain strain pulses at different temperatures are shown in Fig. S14. The main manuscript discusses the variation of the frequency components of the strain pulse in detail.

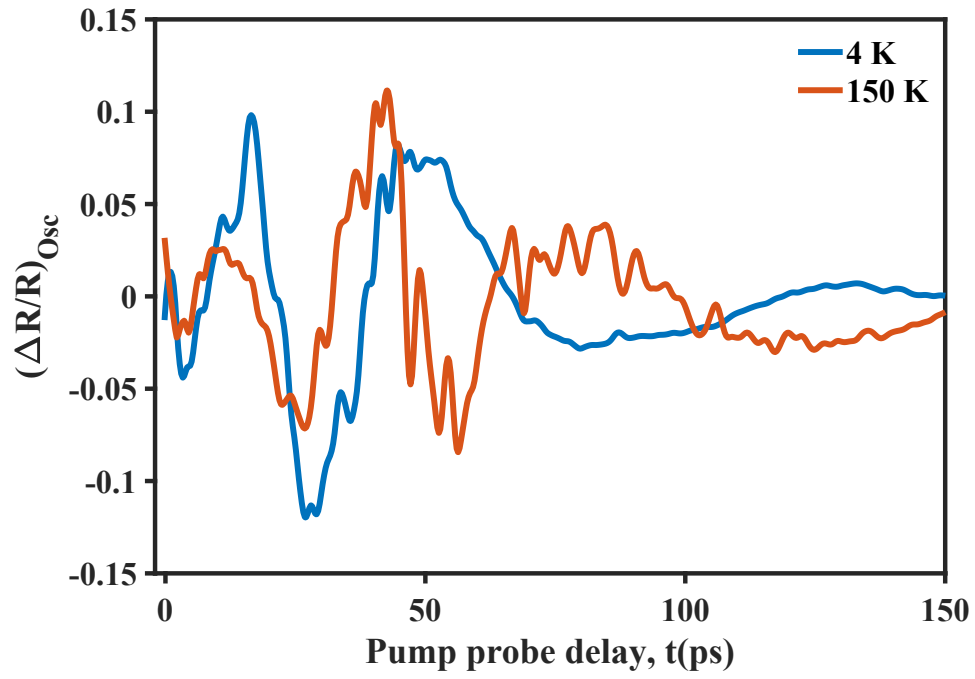


FIG S12: Comparison of strain pulse in ferromagnetic and paramagnetic phases: The figure shows the smoothed time-domain strain pulse for CrSiTe₃ at 4 K (blue solid line) and 150 K (orange solid line) for the first 150 ps after pump excitation

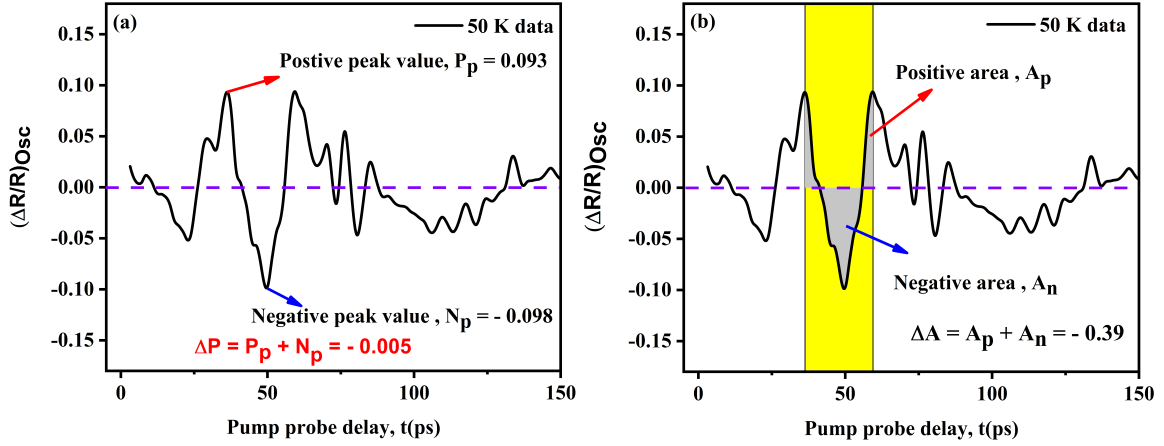


FIG S13: Extraction of (ΔP) and (ΔA) : (a) The peak-to-peak difference (ΔP) of the central peak of strain pulse is shown here. P_p represents the positive peak value (indicated in the solid red arrow) and N_p represents the negative peak value (indicated in the solid blue arrow) of the central peak, respectively. (b) The area difference (ΔA) between the positive area and negative area of the central part of the strain pulse is shown here. A_p represents the positive area (indicated in the solid red arrow) of the main central part of the strain pulse and A_n represents the negative area of the central part of the strain pulse (indicated in the solid blue arrow). Both the areas are shown in shaded grey colour. The purple dashed line marks $y = 0$.

V.b Continuous Wavelet Transform (CWT)

To track the time-dependent behavior of strain pulses, we employed a continuous-wavelet transform (CWT) approach [19, 20, 21]. Leveraging the Gabor mother wavelet, a modified MATLAB code based on a Gaussian function was utilized to achieve this

$$\psi(t/s) = \pi^{-1/4} \left(\frac{1}{ps} \right)^{1/2} \exp \left(-\frac{t^2}{2s^2p^2} + \sqrt{-1} \frac{t}{s} \right), \quad (9)$$

the scaling factor ' s ' corresponds to the inverse of the frequency, while ' p ' is a constant defined as $\pi(2/\ln(2))^{1/2}$. This section outlines the process of calculating the CWT. The wavelet transform of a given time signal, $x(t)$, is represented by

$$CWT(\tau, s) = \frac{1}{\sqrt{|s|}} \int x(t) \psi^*((t - \tau)/s) dt \quad (10)$$

To initiate the wavelet transform, a starting scale (s_{start}) is selected, corresponding to a frequency higher than the signal's highest frequency (determined by FFT). This initial wavelet, denoted as $\psi_{start}(t/s_{start})$, is a compressed version of the signal in the time domain. The cross-correlation of $\psi_{start}(t)$ with $x(t)$ is calculated using equation 10 with $\tau = 0$ (τ is the transnational time). The magnitude of this cross-correlation reflects the similarity between the frequency components of $x(t)$ and $\psi_{start}(t)$. This process is repeated by translating $\psi_{start}(t)$ in the time domain (τ), yielding

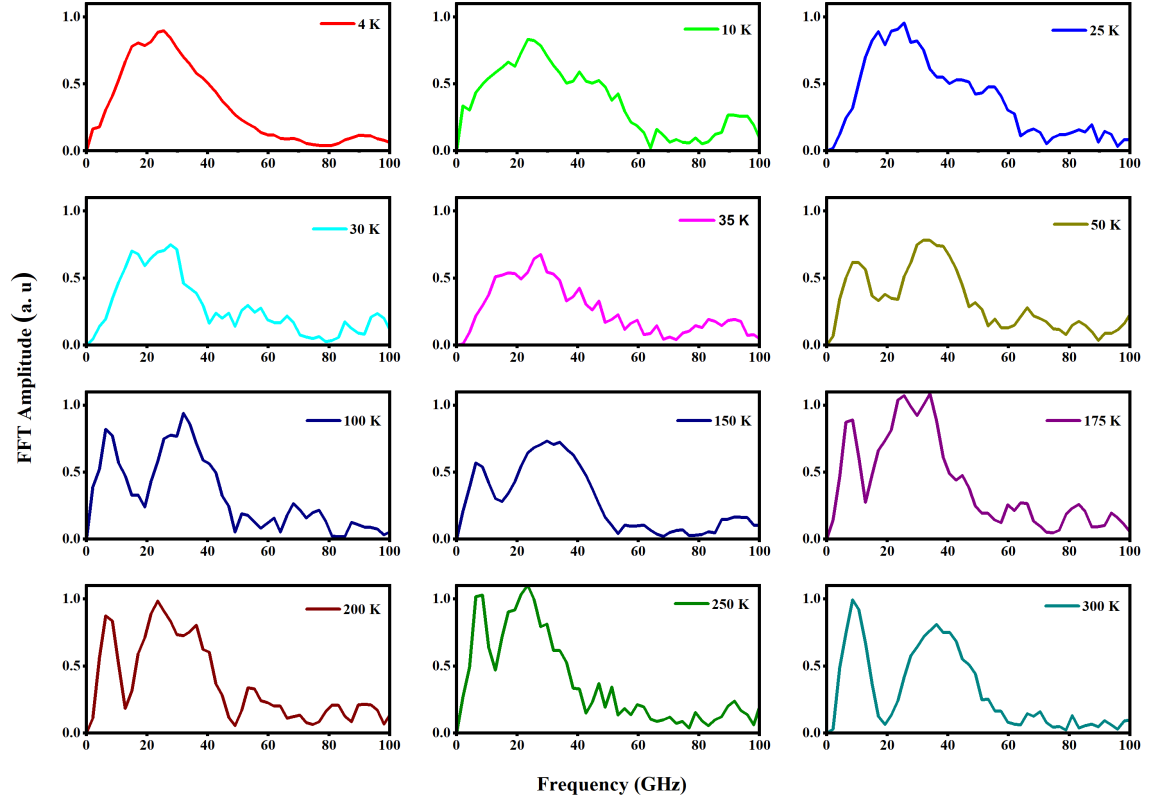


FIG S14: The frequency domain spectrum at various temperatures: This figure shows the FFT amplitude as a function of frequency obtained by fast Fourier transform of time domain strain pulse data for CrSiTe_3 at various temperatures, represented by different colored solid lines.

wavelet coefficients for a specific scale (s) and a range of τ values. The procedure is then iterated for progressively higher scales (s). This results in a collection of wavelet coefficients for $x(t)$ across the time-scale plane. This plane is subsequently transformed into the time-frequency plane. The wavelet transform of a time-domain signal produces a three-dimensional (3D) plot of wavelet coefficients versus frequency and time.

Figure S15 illustrates the evolution of the CWT spectrum (frequency spectrum of the strain pulse) as a function of temperature at various pump-probe delay times obtained from continuous wavelet transform. From the Fig. S15 it is evident that there are two parts in the spectrum: high frequency acoustic part (HFAP) and low frequency acoustic part (LFAP). Both the modes appear within a few picoseconds of pump excitation (data not shown here). The amplitude of HFAP peaks at ~ 50 ps and decays within ~ 150 ps, while the LFAP peaks at ~ 80 ps and then decays within ~ 400 ps, indicates its long-lived nature. In the entire time scale, the nature of the frequency spectrum remains unchanged at $t > 35$ ps. The variation of the acoustic mode frequency with the temperature ($T > T_{3D}$) can be described using the anharmonic decay model given by [22, 23, 24, 25, 26],

$$\omega_i(T) = \omega_i(0) + (\Delta\omega_i)_{anh}(T) \quad (11)$$

where, $\omega_i(0)$ represents the frequency of the i^{th} phonon mode at $T = 0$ K and $(\Delta\omega_i)_{anh}(T)$ is the shift in the frequency of the i^{th} phonon mode due to the anharmonic phonon-phonon coupling, which is given by

$$(\Delta\omega_i)_{anh}(T) = C \left[1 + \frac{2}{\exp\left(\frac{\hbar\omega_i(0)}{2k_B T}\right) - 1} \right] \quad (12)$$

where, C is the constant which signifies the strength of the decay process. \hbar and k_B are the reduced Planck's constant and Boltzmann constant, respectively. This model incorporates cubic anharmonicity, which describes how a high-frequency phonons can decay into two low frequency phonon modes with equal frequencies [23, 24, 25, 26]. The observed frequency shifts of LFAP and HFAP are thus fitted with the anharmonic model and the fit is shown in Fig. 3(b) of the main manuscript. The anharmonic model successfully captures the frequency shifts observed in both the LFAP and the HFAP. The fitting reveals that the zero-frequency values of LFAP and HFAP are $\omega_{LFAM}(0) = 198$ GHz and $\omega_{HFAM}(0) = 225$ GHz, respectively. Notably, the coupling constants C_{LFAP} and C_{HFAP} are determined to be $-17 \times 10^{-4} \text{ cm}^{-1}$ and $-8000 \times 10^{-4} \text{ cm}^{-1}$, respectively. This substantial difference in the magnitudes of C_{LFAM} and C_{HFAM} indicates that the anharmonic coupling is significantly weaker for LFAP compared to HFAP. This is in line with the fact that the high frequency phonons decay to low frequency phonons and hence the decay rate is higher for HFAP; whereas for LFAP, the decay rate is slower as they are already in lower in energy/frequency.

Figure S16 illustrates the evolution of the CWT spectrum (frequency spectrum of the strain pulse) as a function of pump probe delay at various temperatures obtained from continuous wavelet transform.

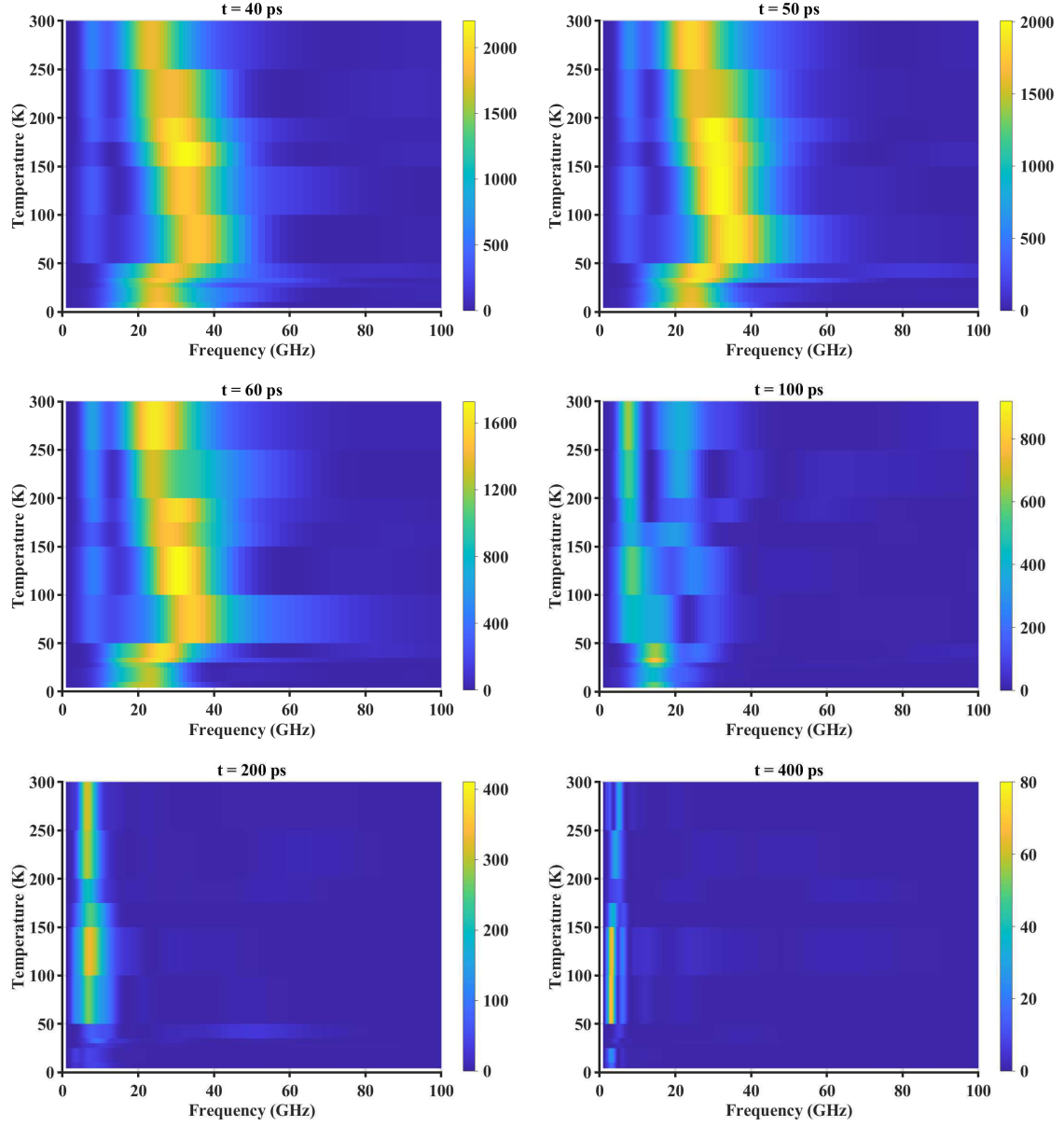


FIG S15: CWT spectra at various pump probe delay times: The evolution of the CWT amplitude with temperature at different pump-probe delay times. For the clarity, CWT spectra at the pump probe delay time 40 ps, 50 ps, 60 ps, 100 ps, 200 ps and 400 ps are shown here

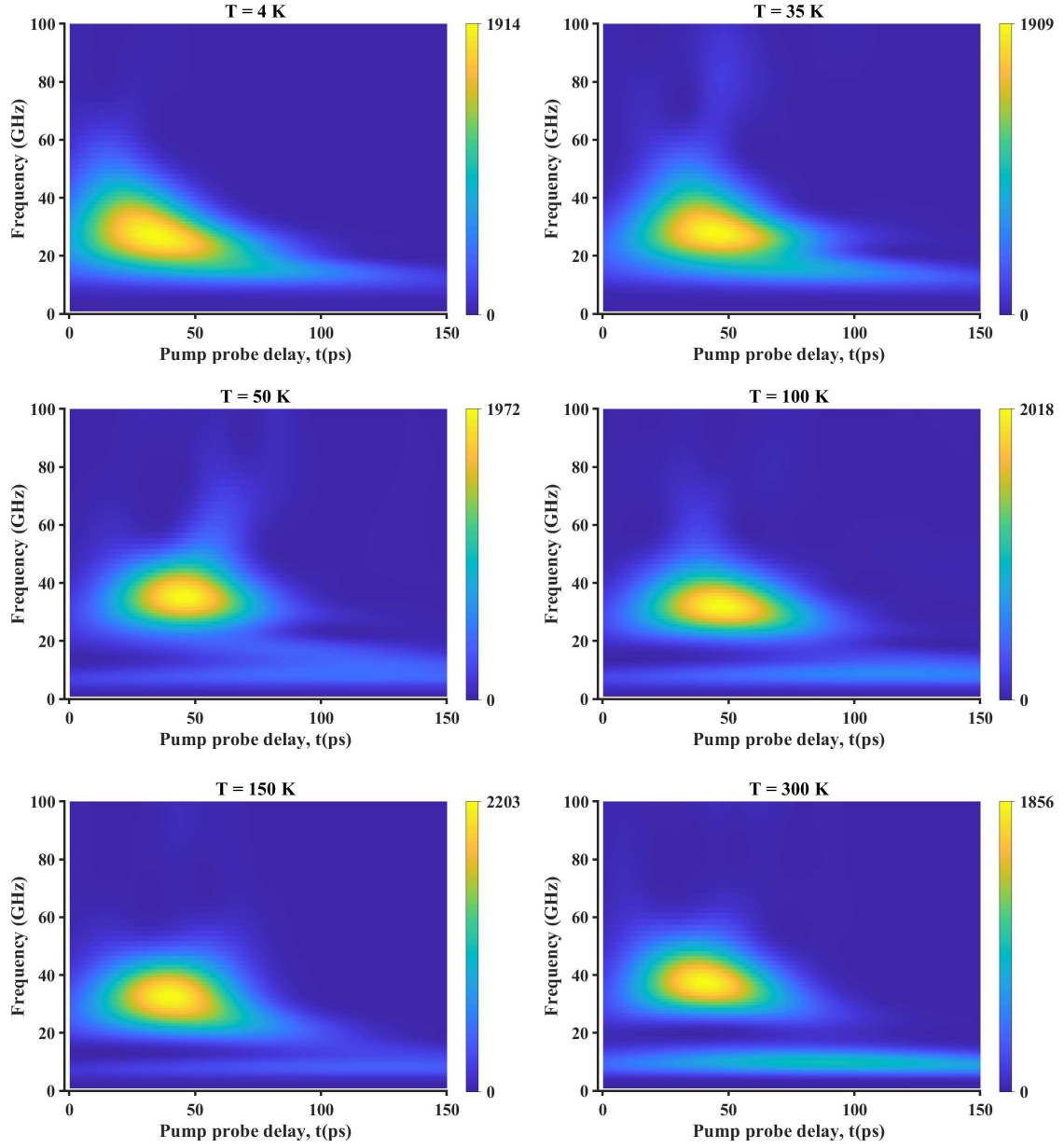


FIG S16: CWT spectra at various temperatures: The evolution of the CWT amplitude with temperature at different pump-probe delay times. For the clarity, CWT spectra at the temperatures 4 K, 35 K, 50 K, 100 K, 150 K and 300 K are shown here.

VI Phenomenological theoretical model

A lattice model of phonons is described by the Lagrangian,

$$\mathcal{L} = \sum_j \left[\dot{Q}_j^2 - \lambda(Q_{j+1} - Q_j)^2 \right] \quad (13)$$

where Q_j is the distortion of the j^{th} atom away from its equilibrium position and λ is the spring constant of the restoring potential. The distortions $Q_j(t)$ are functions of the position index j as well as time t . At this point, we introduce three additional terms in the Lagrangian that represent coupling between the lattice distortions and the magnetic interactions. The magnetic interactions are taken to be of the nearest-neighbor kind: $\vec{S}_j \cdot \vec{S}_{j+1}$. On phenomenological grounds, we allow the magnetic interactions to couple to the linear, quadratic, and gradient components of the distortion, represented by Q_j , Q_j^2 and $(Q_{j+1} - Q_j)^2$, through the coupling constants γ , ξ and χ , respectively.

$$\mathcal{L} = \sum_j \left[\dot{Q}_j^2 - \lambda(Q_{j+1} - Q_j)^2 + \gamma \vec{S}_j \cdot \vec{S}_{j+1} Q_j - \xi \vec{S}_j \cdot \vec{S}_{j+1} Q_j^2 + \chi \vec{S}_j \cdot \vec{S}_{j+1} (Q_{j+1} - Q_j)^2 \right] \quad (14)$$

We treat the magnetic interactions at a mean - field level, replacing the magnetic interactions with their expectation value. From the onset of the LRMO, the expectation value $\langle \vec{S}_j \cdot \vec{S}_{j+1} \rangle$ acquires a uniform non-zero value $M^2(T)$, T being the temperature. Above the T_{3D} , $M^2(T)$ is zero. For the LRMO phase, the Lagrangian takes the form

$$\mathcal{L} = \sum_j \left[\dot{Q}_j^2 - (\lambda - M^2 \chi)(Q_{j+1} - Q_j)^2 + M^2 \gamma Q_j - M^2 \xi Q_j^2 \right] \quad (15)$$

$$= \sum_j \left[\dot{Q}_j^2 - (\lambda - M^2 \chi)(Q_{j+1} - Q_j)^2 - M^2 \xi \left(Q_j - \frac{\gamma}{2\xi} \right)^2 \right] \quad (16)$$

where we have neglected the overall constant. We define a modified distortion $\bar{Q}_j = Q_j - \frac{\gamma}{2\xi}$. In terms of the modified distortion the Lagrangian becomes,

$$\mathcal{L} = \sum_j \left[\bar{Q}_j^2 - (\lambda - M^2 \chi)(\bar{Q}_{j+1} - \bar{Q}_j)^2 - M^2 \xi \bar{Q}_j^2 \right] \quad (17)$$

At this point, one can take the continuum limit of the distortions \bar{Q} being much smaller than the lattice spacing, transforming the discrete index j to the continuum variable x . The distortion $\bar{Q}(x, t)$ then becomes a classical field $\bar{Q}(x, t)$, and the Lagrangian becomes

$$\mathcal{L} = \int_0^L dx \left[(\partial_t \bar{Q}(x, t))^2 - (\lambda - M^2 \chi)(\partial_x \bar{Q}(x, t))^2 - M^2 \xi \bar{Q}(x, t)^2 \right] \quad (18)$$

The equation of motion for this Lagrangian is

$$\ddot{\bar{Q}} = [(\lambda - M^2 \chi) \partial_x^2 - M^2 \xi] \bar{Q} \quad (19)$$

We now introduce the Fourier decomposition of the field $\bar{Q}(x,t)$ in momentum (k) and frequency (ω) domain in terms of the dual models $\tilde{Q}(k, \omega)$:

$$\bar{Q}(x,t) = \int dk d\omega e^{-ikx-i\omega t} \tilde{Q}(k, \omega) \quad (20)$$

In terms of the dual models, the equation of motion becomes

$$[-\omega^2 + (\lambda - M^2\chi)k^2 + M^2\xi] \tilde{Q}(k, \omega) = 0 \quad (21)$$

This equation also reveals the dispersion of the phonons

$$\omega(k) = \sqrt{(\lambda - M^2\chi)k^2 + M^2\xi} \quad (22)$$

where k is the phonon wave-vector. As a consequence, when M is zero (for $T > T_{3D}$), the dispersion simplifies to the expected linear form for acoustic phonons: $\omega(k) = \sqrt{\lambda}k$. When M and the coupling χ are nonzero (for $T < T_{3D}$) but the coupling ξ is negligible, the dispersion retains its linear form. However, the effective spring constant λ is reduced, leading to a softening of the phonon mode.

$$\omega(k) = \sqrt{\lambda_{eff}k}, \quad \lambda_{eff} = \lambda - M^2\chi. \quad (23)$$

For the case $M^2\chi < \lambda$, the coupling between the spin-spin correlations and the gradient component of the distortions leads to the softening of the HFAP across T_{3D} .

The interplay between spin-spin correlations and lattice distortions plays a crucial role in the gapping out the LFAP below a temperature, T_{3D} . This is captured by the dispersion relation (equation (22)) when all interaction parameters (M , χ and ξ) are non-zero.

VII Estimation of coupling constant values

VII.a Estimation of χ from HFAP frequency shift

Between 50 K and 35 K, the central frequency of the HFAP exhibits a 6 GHz decrease in frequency, dropping from 33 GHz to 27 GHz (as shown in Figures 3(b) and 3(c) of the main manuscript). This shift in frequency provides a means to estimate the value of χ , the coupling constant between the spins and the gradient components of the lattice distortion.

For temperature $T > T_{3D} = 50$ K, the dispersion relation for the acoustic phonons in the HFAP takes the form given by,

$$\omega_{50}(k) = \sqrt{\lambda}k \quad (24)$$

here $\omega_{50}(k)$, represents the frequency at $T = 50$ K. For temperature $T < T_{3D} = 50$ K, the dispersion relation takes the form given by,

$$\omega_{35}(k) = \sqrt{(\lambda - M^2\chi)k^2} \quad (25)$$

for negligible ξ , the coupling constant between the spins and the quadratic components of the lattice distortion. Here $\omega_{35}(k)$, represents the frequency at T = 35 K. Taking the ratio between the above equations(18 and 19), we get,

$$\frac{\omega_{50}}{\omega_{35}} = \frac{\sqrt{\lambda}}{\sqrt{(\lambda - M^2\chi)}} \quad (26)$$

Substituting $\frac{\omega_{50}}{\omega_{35}} = \frac{33GHz}{27GHz}$, χ is found to be,

$$\chi \approx \frac{\lambda}{3M^2} \quad (27)$$

With a density of 5.24 g/cm³ and a bulk modulus of 22 GPa [27], the estimated speed of sound in CrSiTe₃ is $v_{HFAP} = \sqrt{\lambda} \sim 2.1 \times 10^3$ m/s. Using the measured magnetization value at T = 35 K, i.e., M = 28.82 $\times 10^3$ A/m, the value of χ is found to be ~ 1.7 mHz m^2/A^2s .

Figure S18 compares the frequency dispersion of HFAP at two distinct temperatures: 50 K and 35 K. In the figure, the red-shift of ~ 6 GHz is shown at $k \sim 9.9 \times 10^5$ cm⁻¹ for parameters of $\chi \sim 1.7$ mHz m^2/A^2s and negligible ξ , highlighting the significant influence of coupling constant χ on the sudden softening of the central frequency of HFAP.

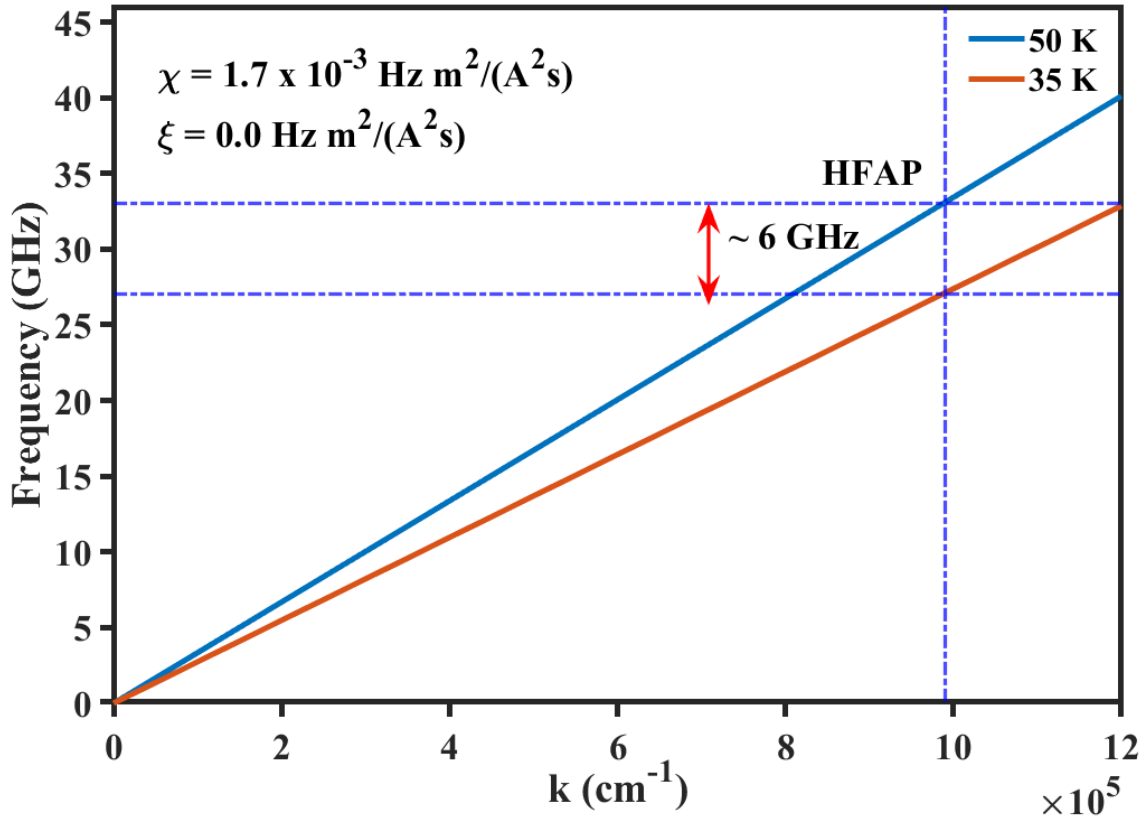


FIG S17: Frequency dispersion of HFAP: This figure shows the dispersion relation of HFAP at two different temperatures: 50 K (blue solid line) and 35 K (red solid line). The shift in the frequency of HFAP is marked by the dark blue dashed lines and indicated by the red double arrow . The parameters χ and ξ used to generate the dispersion spectrum at $T = 35 \text{ K}$ using equation (25) are also shown on the top left corner of the plot.

VII.b Estimation of ξ from LFAP frequency shift

The central frequency of the LFAP at 35K exhibits a blue shift of 7 GHz from its value at 50 K (from 9.6 GHz to 16.6 GHz; Figures 3(b,c)), providing a key tool for estimating ξ .

Since the central frequency of the LFAP (9.6 GHz) at $T = 50$ K is lesser than the central frequency of the HFAP (33 GHz), the speed of the sound is scaled accordingly.

$$v_{LFAP} = 0.29 * v_{HFAP} \quad (28)$$

The dispersion relation for the acoustic phonons in LFAP below $T < T_{3D} = 50$ K, takes of the form,

$$\omega(k) = \sqrt{(\lambda - M^2\chi)k^2 + M^2\xi} \quad (29)$$

and using the similar approach mentioned above and for the negligible value of χ , the value of the ξ is estimated using

$$\xi \approx \frac{0.66\lambda k^2}{M^2} \quad (30)$$

Using suitable values, ξ is found to be ~ 10.2 THz m^2/A^2s .

Figure S18 compares the dispersion relation of the acoustic phonons in LFAP at two distinct temperatures: 50 K and 35 K. A blue shift of ~ 7 GHz in the LFAP frequency is shown by vertical double headed arrow. This shift is accurately reproduced using parameters of $\chi \sim 10.2$ THz m^2/A^2s and negligible ξ (here $\chi \sim 1.7$ mHz m^2/A^2s has a negligible effect on the $\omega(k)$). This highlights the significant influence of coupling constant ξ on the blue shift of the LFAP.

Observe that the central frequency of the high-frequency acoustic component exhibits anharmonic decay behavior within the temperature range of $T=50$ K - 300K, and a notable softening across T_{3D} . Concurrently, the low-frequency acoustic component demonstrates minimal softening within the 50K-300K range, but exhibits a contrasting blue shift across T_{3D} . This implies that both acoustic components could originate from two distinct branches of acoustic phonon. Hence the speed of sound can be different for HFAP and LFAP as in equation 28.

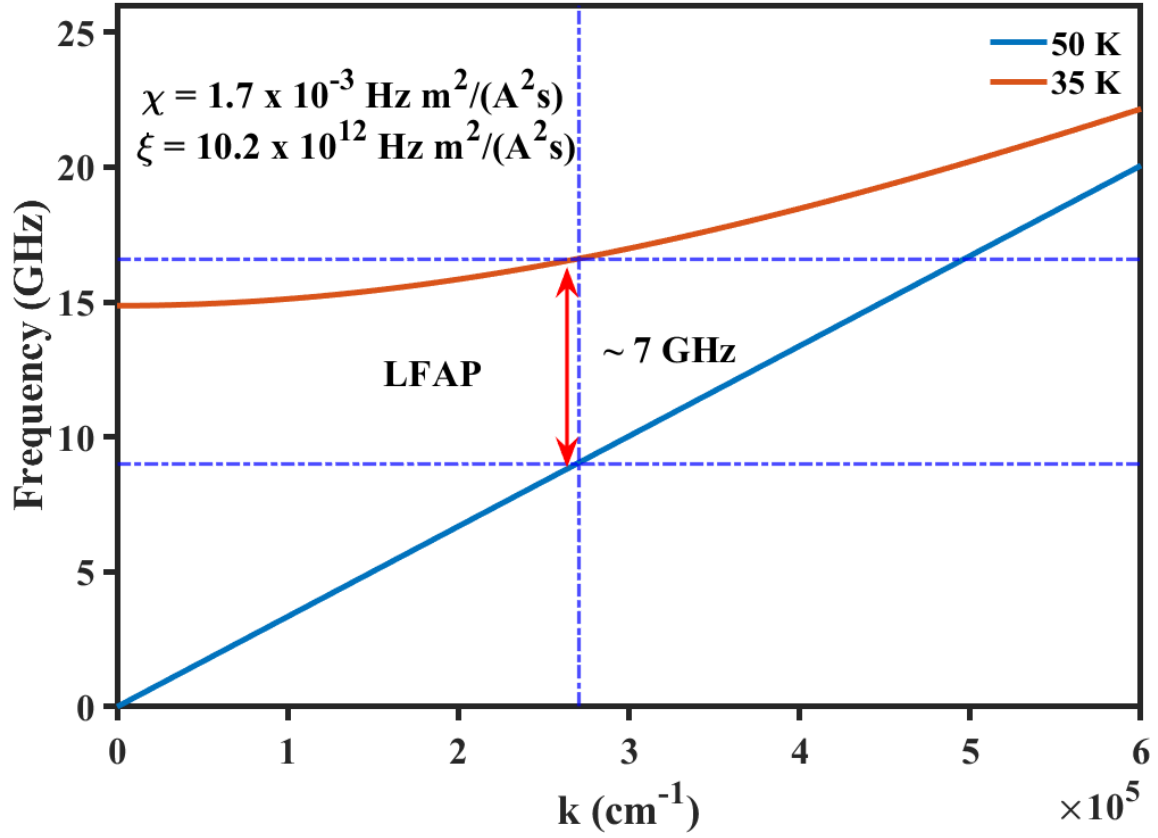


FIG S18: Phonon dispersion relation of the LFAP: This figure shows the dispersion relation of acoustic phonons of LFAP at two different temperatures: 50 K (blue solid line) and 35 K (red solid line). The shift in the frequency of LFAP is marked by the dark blue dashed lines and indicated by the red double arrow. The parameters χ and ξ used to generate the dispersion spectrum at $T = 35 \text{ K}$ are also shown at the top left corner.

VIII Data fitting

The commercial software MATLAB provides many numerical algorithms for solving unconstrained minimization problems. We used the simplex algorithm based on the Nelder-Mead simplex method, which is implemented in MATLAB as the function `fminsearch`.

We fit the experimental data DR to a multi-exponential function, DR_{multi} , to extract the desired parameters. We have used either a bi- or tri-exponential function, as defined in equations 6 and 7, respectively. We minimized the error function $S = DR - DR_{multi}$ to find the best fit. The data and its fit are shown in Fig. S7 (a) and (b). To calculate the error bars, we have used orthogonal distance regression (ODR) approach [28, 29]. The orthogonal ODR algorithm minimizes error function by adjusting both fitting parameters and values of the independent variable in the iterative process. The error bars on the fit parameters are spit out automatically in MATLAB code, we implemented this by calculating the Jacobian matrix followed by the Variance-Covariance Matrix for the fit parameters.

VIII.a Goodness of the fit:

The quality or the goodness of the fit was assessed using both the graphical method and the coefficient of the determination Chi-squared (R^2), which is given by

$$R^2 = \frac{\sum (DR - DR_{multi})^2}{\sum (DR - \langle DR \rangle)^2} \quad (31)$$

Supplementary References

- [1] Casto, L. D., et al. Strong spin-lattice coupling in CrSiTe_3 . *APL Mater.* 3 (2015).
- [2] Milosavljević, A., et al. Evidence of spin-phonon coupling in CrSiTe_3 . *Phys. Rev. B*, 98, 104306 (2018).
- [3] Zhu, Fengfeng, et al. Topological magnon insulators in two-dimensional van der Waals ferromagnets CrSiTe_3 and CrGeTe_3 : Toward intrinsic gap-tunability. *Sci. Adv.* 7, eabi7532 (2021).
- [4] Zhang, Cheng, et al. Hard ferromagnetic behavior in atomically thin CrSiTe_3 flakes. *Nanoscale* 14, 5851-5858 (2022).
- [5] C. P. Weber et. al. Transient reflectance of photoexcited Cd_3As_2 . *Appl. Phys. Lett.* 8, 106, 231904 (2015).
- [6] Jnawali, Giriraj, et al. Band Splitting and Long-lived Carrier Recombination in Ferromagnetic CrSiTe_3 Nanosheets. Preprint at <https://arxiv.org/abs/2109.13440> (2021).
- [7] Kang, S., Kang, S., & Yu, J. Effect of coulomb interactions on the electronic and magnetic properties of two-dimensional CrSiTe_3 and CrGeTe_3 materials. *J. Electron. Mater.* 48, 1441-1445 (2019).

- [8] Kang, S., Kang, S., Kim, H. S., & Yu, J. Field-controlled quantum anomalous Hall effect in electron-doped CrSiTe₃ monolayer. *NPJ 2D Mater. Appl.* 7, 13 (2023).
- [9] Ron, A., et al. Ultrafast enhancement of ferromagnetic spin exchange induced by ligand-to-metal charge transfer. *Phys. Rev. Lett.* 125, 197203 (2020).
- [10] Thomsen, C., et al. Coherent phonon generation and detection by picosecond light pulses. *Phys. Rev. Lett.* 53, 989 (1984).
- [11] Wu, S., et al. Femtosecond optical generation and detection of coherent acoustic phonons in GaN single crystals. *Phys. Rev. B*, 76, 085210 (2007).
- [12] Babilotte, P., et al. Picosecond acoustics in p-doped piezoelectric semiconductors. *Appl. Phys. Lett.* 97 (2010).
- [13] Schmising, C. V. Korff, et al. Ultrafast magnetostriction and phonon-mediated stress in a photoexcited ferromagnet. *Phys. Rev. B*, 78, 060404 (2008).
- [14] von Reppert, Alexander, et al. Unconventional picosecond strain pulses resulting from the saturation of magnetic stress within a photoexcited rare earth layer. *Struct. Dyn.* 7 (2020).
- [15] Mattern, Maximilian, et al. Towards shaping picosecond strain pulses via magnetostrictive transducers. *Photoacoustics* 30, 100463 (2023).
- [16] Ron, A., et al. Ultrafast enhancement of ferromagnetic spin exchange induced by ligand-to-metal charge transfer. *Phys. Rev. Lett.* 125, 197203 (2020).
- [17] Reid, A. H., et al. Beyond a phenomenological description of magnetostriction. *Nat. Commun.* 9, 388 (2018).
- [18] von Reppert, A., et al. Spin stress contribution to the lattice dynamics of FePt. *Sci. Adv.* 6, eaba1142 (2020).
- [19] Torrence, Christopher, & Gilbert P. Compo. A practical guide to wavelet analysis. *Bull. Am. Meteorol. Soc.* 79, 61–78 (1998).
- [20] Hase, Muneaki, et al. The birth of a quasiparticle in silicon observed in time–frequency space. *Nature*. 426, 51-54 (2003).
- [21] Kamaraju, N., Kumar, S., & Sood, A. K. Temperature-dependent chirped coherent phonon dynamics in Bi₂Te₃ using high-intensity femtosecond laser pulses. *EPL*. 92, 47007 (2010).
- [22] Balkanski, M., Wallis, R. F., & Haro, E. Anharmonic effects in light scattering due to optical phonons in silicon. *Phys. Rev. B*, 28, 1928 (1983).
- [23] Orbach, R., & Vredevoe, L. A. The Attenuation of high frequency phonons at low temperatures. *Phys. Phys. Fiz.* 1, 91 (1964).

- [24] Klemens, P. G. Decay of high-frequency longitudinal phonons. *J. Appl. Phys.* 38, 4573-4576 (1967).
- [25] Baumgartner, R., Engelhardt, M., & Renk, K. F. Spontaneous Decay of High-Frequency Acoustic Phonons in CaF_2 . *Phys. Rev. Lett.* 47, 1403 (1981).
- [26] Tamura, S. I. Spontaneous decay rates of LA phonons in quasi-isotropic solids. *Phys. Rev. B*, 31, 2574 (1985).
- [27] Jain, Anubhav, et al. Commentary: The Materials Project: A materials genome approach to accelerating materials innovation. *APL Mater.* 1 (2013).
- [28] Boggs, Paul T., et al. User's reference guide for odrpack version 2.01: Software for weighted orthogonal distance regression. (U.S. Department of Commerce, National Institute of Standards and Technology, 1992).
- [29] Zwolak, J. W., Boggs, P. T., & Watson, L. T. ODRPACK95: A weighted orthogonal distance regression code with bound constraints. *Association for Computing Machinery*, 33 (2004).